

# Blind Image Deconvolution

---

DEEPA KUNDUR AND DIMITRIOS HATZINAKOS



© G. Gove/The Image Bank

The goal of image restoration is to reconstruct the original scene from a degraded observation. This recovery process is critical to many image processing applications. Although classical linear image restoration has been thoroughly studied [1, 2], the more difficult problem of *blind image restoration* has numerous research possibilities.

Our objective in this article is to introduce the problem of blind deconvolution for images, provide an overview of the basic principles and methodologies behind the existing algorithms, and examine the current trends and the potential of this difficult signal processing problem. A broad review of blind deconvolution methods for images is given to portray the experience of the authors and of the many other researchers in this area. We first introduce the blind deconvolution problem for general signal processing applications. The specific challenges encountered in image related resto-

ration applications are explained. Analytic descriptions of the structure of the major blind deconvolution approaches for images then follows. The application areas, convergence properties, complexity, and other implementation issues are addressed for each approach. We then discuss the strengths and limitations of various approaches based on theoretical expectations and computer simulations.

Blind image restoration is the process of estimating both the true image and the blur from the degraded image characteristics, using partial information about the imaging system. In classical linear image restoration, the blurring function is given, and the degradation process is inverted using one of the many known restoration algorithms. The various approaches that have appeared in the literature depend upon the particular degradation and image models [1,2].

In many imaging applications, an observed image  $g(x, y)$ , neglecting additive noise, can be estimated to be the two-dimensional convolution of the true image  $f(x, y)$  with a linear shift-invariant blur, also known as the *point-spread function* (PSF),  $h(x, y)$ . That is,

$$\begin{aligned} g(x, y) &= f(x, y) * h(x, y) \\ &= \sum_{(n,m)} f(n, m)h(x - n, y - m), \end{aligned} \quad (1)$$

$$x, y, n, m \in \mathbb{Z}$$

in which  $*$  denotes the two-dimensional linear convolution operator, and  $\mathbb{Z}$  is the set of integer numbers. The problem of recovering the true image  $f(x, y)$  requires the *deconvolution* of the PSF  $h(x, y)$  from the degraded image  $g(x, y)$ .

Deconvolution is performed for image restoration in many applications such as astronomical speckle imaging [3], remote sensing [4], and medical imaging [5-8], among others. In most situations, the PSF  $h(x, y)$  is assumed to be known explicitly prior to the deconvolution procedure. This problem is known as the classical linear image restoration problem. The long list of deconvolution methods for this situation includes a variety of well known techniques, such as inverse filtering, Wiener filtering, least-squares (LS) filtering, recursive Kalman filtering, and constrained iterative deconvolution methods [1, 9-12].

Unfortunately, in many practical situations, the blur is often unknown, and little information is available about the true image. Therefore, the true image  $f(x, y)$  must be identified directly from  $g(x, y)$  by using partial or no information about the blurring process and the true image. Such an estimation problem, assuming the linear degradation model of Eq. 1, is called *blind deconvolution*. Experience shows that in practice some information is needed to successfully restore the image.

There are several motivating factors behind the use of blind deconvolution for image processing applications. In practice, it is often costly, dangerous, or physically impossible to obtain *a priori* information about the imaged scene. For example, in applications like remote sensing and astronomy, it is difficult to statistically model the original image or even know specific information about scenes never imaged before [3-4]. In addition, the degradation from blurring cannot be accurately specified. In aerial imaging and astronomy, the blurring cannot be accurately modelled as a random process, since fluctuations in the PSF are difficult to characterize [13]. In real-time image processing, such as medical video-conferencing, the parameters of the PSF cannot be pre-determined to instantaneously deblur images [14]. Moreover, on-line

identification techniques used to estimate the degradation may result in significant error, which can create artefacts in the restored image [15].

In other applications, the physical requirements for improved image quality are unrealizable. For instance, in space exploration, the physical weight of a high resolution camera exceeds practical constraints. Similarly, in x-ray imaging, improved image quality occurs with increased incident x-ray beam intensity, which is hazardous to a patient's health [5]. Thus, blurring is unavoidable. In such situations, the hardware available to measure the PSF of an imaging system is often difficult to use. Although these methods work well to identify the PSF, they are esoteric, which limits their wide use [8, 13]. Blind deconvolution is a viable alternative for improving image quality without requiring complicated calibration methods.

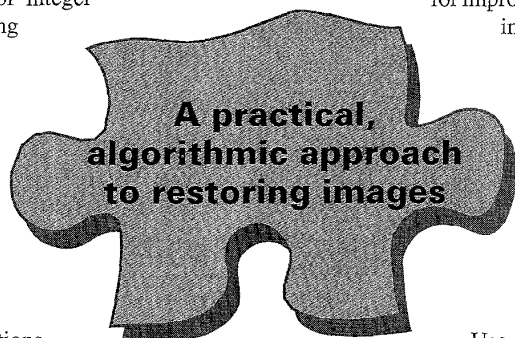
Finally, for applications such as astronomy, adaptive-optics systems may be used to compensate for blurring degradations, although the high cost of these systems makes imaging impractical for some observational facilities.

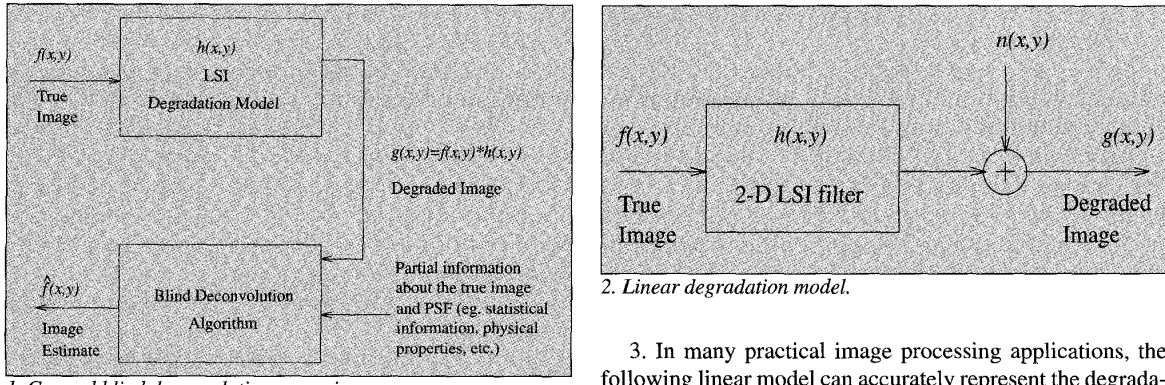
Use of less expensive, partially compensating systems may result in phase errors. In either situation, post-processing such as blind deconvolution is required for improved image quality [16-17].

It is clear that classical image restoration methods that assume a known PSF are not suitable for many *real* image processing situations. In these cases, an algorithmic approach to combined blur identification and image restoration is required. In this sense, blind deconvolution is a practical method for image restoration. Indeed, existing research in the area [8, 13, 15, 18-51], has shown its worth.

## Problem Formulation

The general blind deconvolution problem refers to the task of separating two convolved signals,  $f$  and  $h$ , when both the signals are either unknown or partially known. This important problem occurs in many applications in addition to image restoration, such as seismic data analysis, blind equalization of communication channels, transmission monitoring, and echo cancellation in wireless telephony [18, 52-53]. The basic approach for all cases involves using the partial information available about the scheme as a reference to deconvolve the received signal components. The partial information can be in the form of physical properties of the true signal, such as finite support and nonnegativity found in image processing, or it can be in the form of statistical information such as entropy used for seismic data analysis, or the probability density function (pdf) of the true signal used for equalization of communication channels. In most blind deconvolution techniques, the partial information is incorpo-





1. General blind deconvolution scenario.

rated into an optimality criterion, which is minimized (or maximized) to find estimates of the components (or their inverses). Figure 1 depicts the general blind deconvolution scenario.

There are some important characteristics of the problem of blind deconvolution for images. These include:

1. The true image and PSF must be *irreducible* for an unambiguous deconvolution. An irreducible signal is one which cannot be exactly expressed as the convolution of two or more component signals, on the understanding that the two-dimensional delta function is not a component signal. This is an important property of the system because if either the true image or the PSF are reducible then the solution to the problem is ambiguous. For example, if  $h(x, y)$  and  $f(x, y)$  are reducible and  $h(x, y) = h_1(x, y) * h_2(x, y)$  and  $f(x, y) = f_1(x, y) * f_2(x, y)$ , then

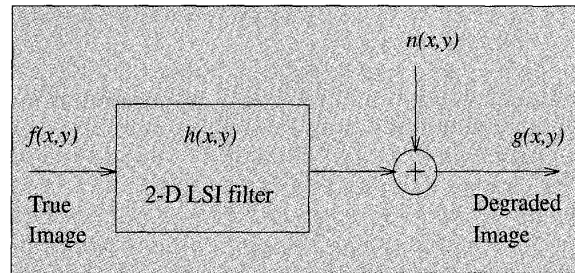
$$g(x, y) = f_1(x, y) * f_2(x, y) * h_1(x, y) * h_2(x, y) \quad (2)$$

There are four components to  $g(x, y)$ ; ambiguity occurs for image restoration in deciding which component(s) belong to the true image and to the PSF.

2. In classical linear image restoration, the goal is to obtain an estimate as close as possible to the true image. Ideally,  $\hat{f}(x, y) = f(x, y)$ , where  $\hat{f}(x, y)$  is the image estimate from the restoration procedure. However, in blind image restoration, the goal is to obtain a scaled, shifted version of the original image. That is,

$$\hat{f}(x, y) = Kf(x - D_x, y - D_y) \quad (3)$$

where  $\hat{f}(x, y)$  is the estimate of the image from the blind deconvolution procedure, and  $K, D_x$  and  $D_y$  are arbitrary real constants.  $K, D_x$ , and  $D_y$  cannot be recovered by blind deconvolution algorithms in general [19]. After blind deconvolution is performed, however, the gain and shifting can be recovered by using additional constraints, such as information that the mean value of the image is preserved (i.e.,  $\sum_{\forall(x,y)} h(x, y) = 1$ , or information about the location of the support of the image).



2. Linear degradation model.

3. In many practical image processing applications, the following linear model can accurately represent the degradation of the true image.

$$g(x, y) = f(x, y) * h(x, y) + n(x, y) \quad (4)$$

where  $g(x, y)$  is the degraded image,  $f(x, y)$  is the true image,  $h(x, y)$  is the PSF, and  $n(x, y)$  represents the additive noise. The noise term is important because in practical imaging situations, additive noise is not negligible. Common types of noise are 1) electronic noise, resulting from the thermal motion of electrons in the electronic components of the imaging system, 2) photoelectric noise, due to the statistical nature of light and photoelectric conversion process in the image sensor, 3) film grain noise, from the randomness of silver halide grains in the film used for recording, and 4) quantization noise, which occurs during image digitization. Figure 2 provides an overview of the linear degradation model for images. The problem of blind image restoration, for situations in which additive noise is present, closely follows the blind deconvolution problem described for the noiseless case.

In addition to the above considerations, some practical constraints for image processing applications include:

- The image restoration problem is, in general, *ill-conditioned*; a small perturbation of the given data produce large deviations in the resulting solution [54, 55]. Since the process of deconvolution attempts to restore the image by some method of inversion of the PSF, the problem is often ill-conditioned owing to the existence of the additive noise. The direct inverse of the blur transfer function usually has a large magnitude at high frequencies, so excessive amplification of the noise results at these frequencies.
- Exact deconvolution is impossible as a result of the presence of additive noise in the imaging system. Only statistical information about the noise may be available, therefore, subtraction of the noise  $n(x, y)$  from the degraded image  $g(x, y)$  is impossible. In addition, the additive noise makes  $g(x, y)$ , in general, irreducible. Thus, only an approximate deconvolution can be performed [19].
- The solution may not be unique. Since only partial information about the imaging process is used to formulate an optimality criterion, many different estimates of the true image and PSF may lead to an optimal solution. An appropriate solution may be chosen through proper initialization

of the algorithm or by making additional assumptions on the imaging system [52].

- There exists a poor compromise among computational complexity, convergence properties, and portability of the algorithm for the existing blind deconvolution methods. The relative importance of each of the above factors depends on the particular imaging application. For example, in real-time image restoration, reducing computational complexity and convergence speed is of the utmost importance, but for medical imaging applications, the reliability of the solution is the primary consideration. The challenge is to design a method that exhibits the most appropriate compromise among computation complexity, reliability, and portability for a given application [42].

## Existing Approaches

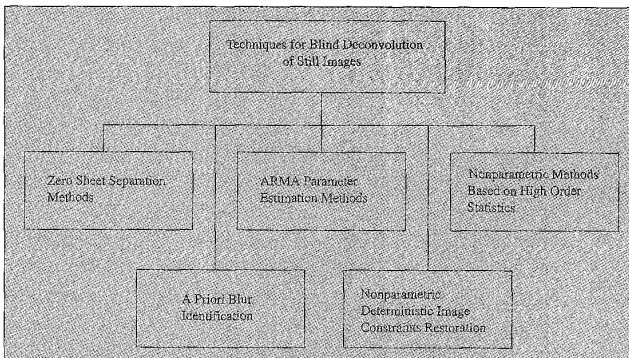
There are two main approaches to blind deconvolution of images:

1. Identifying the PSF separately from the true image, in order to use it later with one of the known classical image restoration methods. Estimating the PSF and the true image are disjoint procedures. This approach leads to computationally simple algorithms.
2. Incorporating the identification procedure with the restoration algorithm. This merge involves simultaneously estimating the PSF and the true image, which leads to the development of more complex algorithms.

A possible classification of the existing blind deconvolution methods for images is depicted in Figure 3. *A priori* blur identification techniques fall under the first approach, and the remaining classes of methods fall under the second. This section describes each class of algorithms, discusses their strengths and limitations, and highlights potential application areas.

### Zero Sheet Separation

The method of zero sheets has received attention because it provides valuable insight into the blind deconvolution problem in multiple dimensions. Lane and Bates [19] have shown that any degraded image  $g$ , formed by convolving several



3. Classification map of existing blind deconvolution techniques for images.

individual components  $f_1, f_2, \dots, f_n$ , having compact support, is automatically deconvolvable provided its dimension is greater than one. Their argument rests on the analytic properties of the Z-Transform (ZT) in multiple dimensions. The zeros of the ZT of a  $K$ -dimensional component  $f_i$  is almost always continuous and lies on a  $(2K-2)$ -dimensional hypersurface. The zero sheets can very rarely possess singularities; the relevant details are provided in [63]. By separating these hypersurfaces, we can recognize the individual components up to a complex scale factor.

The following assumptions are made about the imaging system [19]:

- There is no additive noise present in the imaging system. That is,

$$g(x, y) = f(x, y) * h(x, y)$$

- The true image  $f(x, y)$  and the PSF  $h(x, y)$  have finite support.
- $f(x, y)$  and  $h(x, y)$  are irreducible. From the analytic properties of the ZT for a signal of dimension greater than one, this implies that the ZT of each  $f(x, y)$  and  $h(x, y)$  is zero on a single continuous surface, which is called a zero sheet [19].
- The zero sheets of  $f(x, y)$  and  $h(x, y)$  are distinct in the sense that they can intersect only at discrete points in the 4-dimensional space (assuming that we are dealing with two-dimensional signals).

Based on the assumptions stated above, Lane and Bates have shown that blind deconvolution of a single multidimensional image is possible. There is no need to invoke either a reference image or a sequence of differently blurred images. The lack of the fundamental theorem of algebra for polynomials of order greater than one indicates that multidimensional polynomials are not generally factorizable. In the case of the convolution of two components,  $g(x, y) = f(x, y) * h(x, y)$ , the following relation holds:

$$G(z_1, z_2) = F(z_1, z_2)H(z_1, z_2) \quad (5)$$

where capital letters represent the ZT's of their lower-case counterparts. Since Eq. 5 shows that the polynomial  $G(z_1, z_2)$  is factorizable, the blind deconvolution problem in two-dimensions is equivalent to factoring the two-dimensional polynomial  $G(z_1, z_2)$ . The factors will represent  $F(z_1, z_2)$  and  $H(z_1, z_2)$  scaled by an arbitrary complex constant. In the image space domain, this translates to determining  $f(x, y)$  and  $h(x, y)$  up to a scale factor and shift, which is the goal of the blind deconvolution of images. The main steps of this technique for a two-dimensional image are outlined in Table 1. “ZT factor” denotes any scaled version of either  $F(z_1, z_2)$  or  $H(z_1, z_2)$ , and “FT factor” denotes a “ZT factor” evaluated only on the unit circles.

The zero sheet separation technique is helpful in providing insight into the blind deconvolution problem. Based on the concept of zero sheets, it has been shown that image processing in three or more dimen-

sions is an over-determined problem if the image or the Fourier amplitude is measured at the Nyquist rate [21]. The zero sheet method may also be used to simultaneously deconvolve more than two components, and can determine the number of irreducible signals a given signal is composed of.

Although the concept of zero sheets is helpful conceptually, there exist many practical drawbacks to this approach of blind deconvolution. Basically, the algorithm is highly sensitive to noise, the fastest algorithm to date [20] has a computational complexity of  $O(Ng^4)$ , where  $Ng$  is the number of pixels of the blurred image, and the algorithm is prone to numerical inaccuracy for large data sizes. In the next section we introduce a class of more practical blind deconvolution methods with considerably fewer computational requirements.

### A Priori Blur Identification Methods

#### The General Approach

*A priori* blur identification methods perform blind deconvolution by identifying the PSF prior to restoration. This general class of techniques makes assumptions on the characteristics of the PSF such as symmetry, and availability of a known parametric form of the blur. Popular parametric models include PSFs resulting from linear camera motion or an out-of-focus lens system. Based on these assumptions, an attempt is made to completely characterize the PSF using special features of the true/blurred image. These features may include a point source against a uniform background found in applications such as astronomical speckle imaging [3], edges common in non-destructive industrial x-ray imaging [22], and frequency domain nulls found in situations in which the blurring results from camera misfocus and linear motion, among others [23-26]. Once the PSF has been completely identified, one of the classical restoration techniques is used to estimate the true image.

*A priori* blur identification techniques are the simplest class of blind deconvolution methods to implement and have low computational requirements. They are applicable to situations in which the true image is known to possess special features, and/or when the PSF is known to be of a special parametric form. For more general situations or when less information is available other deconvolution algorithms must be used.

Many methods of this class use specific features about the true image, such as point sources or edges, to estimate the PSF. We will concentrate on the most popular methods of this class that use the frequency domain nulls of the degraded image to perform blind deconvolution [23-24]. The following section provides an overview of this approach.

#### Blur Identification Based on the Frequency Domain Zeros

The following degradation model, which neglects noise, i.e.,

$$g(x,y) = f(x,y) * h(x,y), \quad x,y \in \mathbb{Z}$$

is assumed for the imaging system. Taking the discrete Fourier transform of each side results in the following frequency domain relationship, in which capital letters denote

**Table 1: Summary of the Zero Sheet Separation Algorithm**

#### I) Polynomial Root Association and Grouping

1.  $z_1 = z_0$  is set ( $z_0 = 1$  is usually chosen). The roots of the resulting polynomial in  $z_2$  are computed with a standard root solver. The roots are denoted by  $Z_i(z_0)$ ,  $i = 1, 2, \dots, N_r$ , where  $N_r$  is the total number of roots.

2. The roots are divided into two groups,  $S_1, S_2$ , which each contain roots belonging to the same ZT factor.  $Z_i(z_0)$  is assigned to  $S_1$ .

For each pair of roots  $(Z_i(z_0), Z_j(z_0))$  for  $i \neq j$ ,

a. The complex variable,  $z_1$ , is moved along a mathematically derived path that causes  $Z_i(Z_0)$  and  $Z_j(Z_0)$  to merge at common points.

b. At the point where the pair of roots merge, a test of analyticity is performed to determine whether or not the roots belong to the same ZT factor. They are grouped into  $S_1$  and  $S_2$  accordingly.

#### II) Root Tracking and FT Factor Generation

1. The location of the roots in  $S_1$  and  $S_2$  are tracked as  $z_1$  is sequentially moved to discrete points on the unit circle.

2. At each point on the unit circle, a column of each FT factor matrix is generated.

#### III) I and II are repeated switching the roles of $z_1$ and $z_2$ .

#### IV) FT Factor Matrix Equalization and Deconvolution

1. The resulting two FT factor matrices are scaled and merged.

2. The image estimate  $\hat{f}(x,y)$  and the PSF estimate  $\hat{h}(x,y)$  are generated by taking the inverse fast-Fourier transform (FFT) of the FT factor matrices.

the discrete Fourier transform of their lowercase counterparts:

$$G(u,v) = F(u,v)H(u,v), \quad u,v \in \mathbb{R} \quad (6)$$

From Eq. 6, one sees that the zeros of  $G(u,v)$  are collectively the zeros of  $F(u,v)$  and  $H(u,v)$ .

It is assumed that the PSF is of a known parametric form and that given its frequency domain zeros (i.e., the zeros of  $H(u,v)$ ), the associated parameter value(s) can be uniquely determined. The following PSFs, commonly encountered in practice, are completely characterized by their frequency domain zeros [23]:

#### 1. Horizontal camera motion blur of length $2d$ :

$$h(x,y) = \begin{cases} 0 & y \neq 0 \quad -\infty \leq x \leq \infty \\ \frac{1}{2d} & y = 0 \quad -d \leq x \leq d \end{cases} \quad (7)$$

**Table 2: Summary of *a priori* Blur Identification Techniques Making Use of Frequency Domain Zeros**

**I**) The image is partitioned in smaller (possibly overlapping) frames, each of which is large enough to contain the PSF. Each subsection is windowed to reduce edge effects. The following model, after windowing, holds approximately:

$$g_i(x,y) = f_i(x,y) * h(x,y) + n_i(x,y), i = 1, 2, \dots, N_p \quad (1)$$

where  $N_p$  is the total number of partitioned subsections. The presence of additive noise is included in the model.

**II**) The frequency domain nulls of  $h(x,y)$  are identified.

1. The power spectrum of each subsection  $g_i(x,y)$ , defined as

$$\Phi_{g_i}(u,v) = |\mathcal{F}\{g_i(x,y)\}|^2 \quad (2)$$

$$= \Phi_{f_i}(u,v)|H(u,v)|^2 + \Phi_{n_i}(u,v) \quad i = 1, 2, \dots, N_p \quad (3)$$

is calculated using the method proposed by Welch.  $\Phi_{f_i}(u,v)$  and  $\Phi_{n_i}(u,v)$  are the power spectra of  $f_i(x,y)$ , and  $n_i(x,y)$ , respectively, and  $\mathcal{F}\{\cdot\}$  represents the fast Fourier Transform (FFT) operator.

2. The average of the power spectra is calculated.

$$\Phi_g(u,v) = \sum_{i=1}^{N_p} \Phi_{g_i}(u,v) \quad (4)$$

This averaged quantity retains the flavor of  $|H(u,v)|$ , since it is present in each of the averaged subsections. The contribution of  $f_i(x,y)$  and  $n_i(x,y)$ , on the other hand, will vary from section to section, resulting in a much smaller contribution to the average. The “small” values of  $\Phi_g(u,v)$  will correspond strongly to the zeros of  $H(u,v)$ .

3. The power cepstrum defined as

$$c_g(p,q) = \mathcal{F}\{\log(\Phi_g(u,v))\} \quad (5)$$

is calculated. Periodic dips in the amplitude of  $\Phi_g(u,v)$  lead to large negative spikes in  $c_g(p,q)$ . For example, in linear motion, the PSF dips are periodic and  $1/d$  apart. This results in a negative spike in  $c_g(p,q)$  a distance  $d$  from the origin. The angle of the spike denotes the direction of the motion blur. The circular symmetry of the out-of-focus PSF results in rings of spikes in the cepstrum, which reflect the approximately radially periodic nature of its frequency domain zeros.

**III**) Using the location of the spikes of the quantity  $c_g(p,q)$ , the type of blur (out-of-focus or linear camera motion) is identified, and the corresponding parameter value is estimated using visual inspection or a threshold procedure.

**IV**) The true image is deconvolved using the estimated PSF with one of the classical linear image restoration methods.

This type of PSF has frequency domain zeros on lines perpendicular to the direction of the blur which are spaced at intervals of  $1/d$ .

## 2. Defocused lens system with a circular aperture:

$$h(x,y) = \begin{cases} 0 & \sqrt{x^2 + y^2} > r \\ \frac{1}{\pi r^2} & \sqrt{x^2 + y^2} \leq r \end{cases} \quad (8)$$

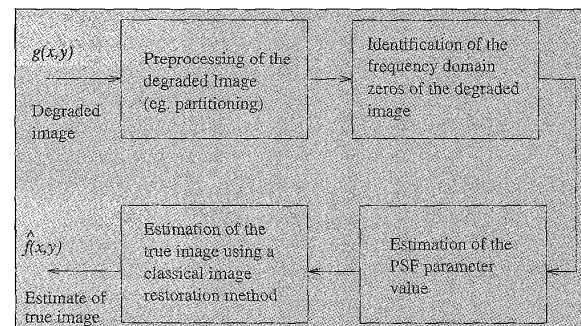
The corresponding frequency zeros are concentric circles about the origin that are nearly periodic in  $r$ .

Given the zeros of  $G(u,v)$  and a parametric form of the PSF, the problem of blind deconvolution involves distinguishing the zeros of  $H(u,v)$  from those of  $F(u,v)$ . A partitioning procedure explained in [23] and summarized in the beginning of Table 2 can be used. Once the locations of the zeros of  $H(u,v)$  are identified, the parameter value(s) of the PSF are estimated (i.e.,  $d$  in Eq. 7 or  $r$  in Eq. 8 are estimated, if the PSF is due to camera motion or defocus). Given the estimated PSF, a classical image restoration algorithm is used to obtain an estimate of the true image.

This method is summarized in Fig. 4. The PSF is assumed to be at least two orders of magnitude less in extent than the true image. The specific algorithm is provided in Table 2.

This blind deconvolution approach does not consider the presence of the additive noise in the degraded image; the noise has the effect of masking the frequency domain nulls of  $g(x,y)$ . The algorithm is, therefore, sensitive to noise, and works well for high signal-to-noise ratios (SNR) [24]. Modifications have been made to make the method more robust to noise by using the bicepstrum instead of the power cepstrum. These methods are successful in suppressing noise, but require the image data to be large (at least 512 x 512 pixels large) for good results [24].

The method of blur identification based on frequency domain zeros is one of the most popular and successful methods because of its computational simplicity and reliability. It has been shown to work well in real situations. The major limitation is that a parametric form of the PSF is required to be known. In addition, for applications like x-ray or astronomical imaging, where the PSF is often Gaussian,



**4. Summary of blur identification methods based on frequency domain nulls.**

frequency domain zeros of  $H(u,v)$  do not exist. For such situations, another blind deconvolution method must be used. The next section introduces a class of methods that requires fewer assumptions on the PSF, but imposes constraints on the true image.

### ARMA Parameter Estimation Methods

Blind deconvolution using ARMA parameter estimation methods involves modeling the true image as a two-dimensional autoregressive (AR) process and the PSF as a two-dimensional moving average (MA) process. Based on these models, the resulting blurred image is represented as an autoregressive moving average (ARMA) process. Identifying the ARMA parameters allows us to identify the true image and PSF.

The existing methods of this class differ in how the ARMA parameters are estimated. Techniques based on second-order statistics, such as maximum-likelihood (ML) estimation [27–30], generalized cross-validation (GCV) [31], and neural networks [32] have been proposed. High order statistics (HOS) methods have also been used for ARMA estimation [33]. The ML and GCV methods are the most successful for image processing applications and are discussed later.

#### AR Model of the True Image

The true image is modelled as a two-dimensional autoregressive (AR) process represented by:

$$f(x,y) = \sum_{\substack{(l,m) \in R_a \\ (l,m) \neq (0,0)}} a(l,m)f(x-l,y-m) + v(x,y) \quad (9)$$

where the parameter  $a(0,0)$  equals 1,  $f(x,y)$  is the true image, and  $v(x,y)$  is the modelling error which is a zero-mean homogeneous noise process with covariance matrix  $Q_v$ , which is statistically independent of  $f(x,y)$ .

Existing methods based on second-order statistics assume  $v(x,y)$  is Gaussian; however, HOS-based methods assume  $v(x,y)$  is non-Gaussian. The AR model coefficients  $\{a(l,m)\}$  of support,  $R_a$ , are chosen to minimize the variance of  $v(x,y)$  denoted by  $\sigma_v^2$ . (The support of a two-dimensional signal is the smallest rectangle encompassing all non-zero components of the signal.) A more compact version of Eq. 9 can be derived by lexicographically ordering the two-dimensional signals and using matrix-vector notation [30]:

$$f = Af + v \quad (10)$$

(Lexographic ordering is used to map an  $M \times N$  matrix to a column vector. This row-ordered vector is defined as  $\mathbf{x}^T = [x(1,1) \ x(1,2) \dots x(1,N) \ x(2,1) \dots x(2,N) \dots x(M,1) \dots x(M,N)]^T$ , where  $x(l,m)$  is the  $(l,m)$ th element of the  $M \times N$  matrix.)

The model of the true image in Eq. 10 is valid in applications such as photography where the true images are generally smooth and homogeneous [57]. Only three AR coefficients  $\{a(0,1), a(1,0), a(1,1)\}$  are sufficient to reasonably model a photographic image. In fact, the model may be represented as a process in which the autocorrelation function consists of a separable exponentially decaying sequence and a more simplified AR model may be used where  $a(0,1) = \rho_v$ ,  $a(1,0) = \rho_h$ , and  $a(1,1) = \rho_v \rho_h$  and  $0 < \rho_v \rho_h < 1$  [57]. The model of Eq. 10 is also appropriate for texture images, but model order selection is required to estimate the number of AR coefficients. The AR model is not valid for situations in which the true image has abrupt changes in local image characteristics, such as for edges.

#### ARMA Model of the Blurred Image

In most practical situations, the PSF is of finite extent and its effect on the true image can be modeled as that of a two-dimensional FIR filter. From the linear degradation model of Eq. 4, the degraded image  $g(x,y)$  can be expressed as:

$$g(x,y) = \sum_{(l,m) \in R_h} h(l,m)f(x-l,y-m) + n(x,y) \quad (11)$$

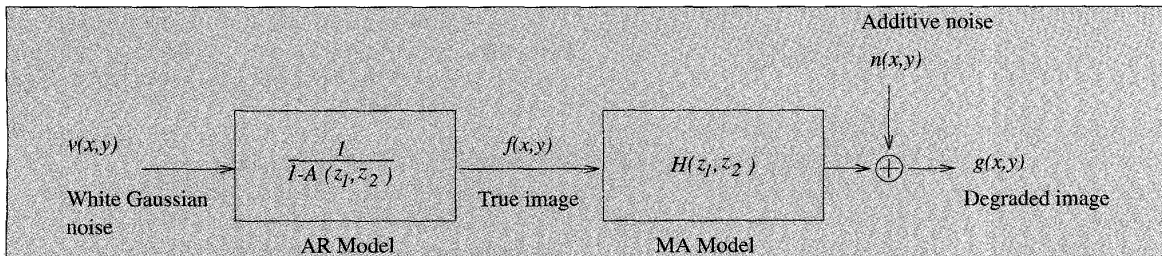
where  $R_h$  is the finite support of the PSF  $h(x,y)$ , and  $n(x,y)$  is the additive noise of the imaging system assumed to be zero-mean Gaussian with covariance  $Q_n$ . Once again, using matrix-vector notation, Eq. 11 becomes:

$$g = Hf + n \quad (12)$$

Rearranging Eq. 10, substituting into Eq. 12 and rearranging yields:

$$g = H(I-A)^{-1}v + n \quad (13)$$

where  $I$  is the identity matrix. A complete model for the blurred image using Eq. 13 is given in Fig. 5, where capital letters denote Z-transforms of their lowercase counterparts. Therefore, the problem of blind deconvolution consists of estimating  $a(l,m)$  for  $(l,m) \in R_a$  and  $h(l,m)$  for  $(l,m) \in R_h$



5. ARMA model of the blurred image.

from  $g(x,y)$ . Once  $h(l,m)$  is determined, one of the classical linear image restoration methods can be used to estimate the true image.

#### Parametric Model of the PSF

The practical difficulties with estimating  $\{a(l,m), h(l,m)\}$  using Eq. 13 include high computational complexity for PSFs with large support, instability of the estimation algorithms, and non-unique solutions, among others [30]. To overcome these problems, the following additional assumptions are commonly made on the PSF by existing second-order statistics methods.

- The PSF is positive, and the mean value of the true image is preserved in the degradation process. That is,

$$\sum_{(l,m) \in R_h} h(l,m) = 1 \quad (14)$$

the use of these assumptions limits the number of possible ambiguous solutions to the problem.

- The PSF is symmetric and zero-phase. These assumptions are made for the stability and the uniqueness of solution of the estimation algorithms.
- The PSF has a known parametric form consisting of only a few parameters. Use of such models significantly lowers the computational complexity.

Examples of blurs which conform to the above properties include the linear motion and the out-of-focus PSFs of Eqs. 7 and 8, respectively. Based on these assumptions, the specific problem of model order selection (i.e., estimating  $R_a$  and  $R_h$  is avoided).

#### The Maximum-Likelihood Approach

The maximum-likelihood (ML) methods attempt to derive restoration filters by estimating the PSF, variance of the additive noise  $n(x,y)$ , and the AR model coefficients of the original image. Thus, the problem consists of estimating the parameter set

$$\Theta = \{ \{h(l,m)\}, \{a(l,m)\}, \sigma_n^2, \sigma_v^2 \}$$

from  $g(x,y)$ , assuming that the given models of the true image and PSF hold.  $\sigma_n^2$  and  $\sigma_v^2$  are the variances of  $n(x,y)$ , and  $v(x,y)$ , respectively.

An estimate of the parameters is made such that the probability or likelihood of receiving the observed image given the parameter set,  $\Theta$ , is maximized. The ML estimator is given by:

$$\hat{\Theta}_{ml} = \arg \left\{ \max_{\Theta \in \Theta} L(\Theta) \right\} = \arg \left\{ \max_{\Theta \in \Theta} \log p(g; \Theta) \right\} \quad (15)$$

where  $L(\Theta)$  denotes the log-likelihood function of  $\Theta$ ,  $\Theta$ , specifies the range of elements of  $\Theta$ , and  $p(g; \Theta)$  is the probability density function (pdf) of  $g$  for a given  $\Theta$ .

Since both  $n$  and  $v$  are assumed to be zero-mean Gaussian processes,  $g$  is also zero-mean and Gaussian, because it is a linearly filtered version of both  $n$  and  $v$ . In fact, it can be

shown that the pdf of  $g$  conditioned on  $f, H$ , and the covariance matrix of  $n$ ,  $Q_n$ , is given by

$$p(g|f, H, Q_n) = \frac{1}{\sqrt{2\pi^{N^2} \det Q_n}} \exp \left[ -\frac{1}{2} (g - Hf)^T Q_n^{-1} (g - Hf) \right] \quad (16)$$

In addition, the pdf of  $f$ , given  $A$  and the covariance matrix of  $v$ ,  $Q_v$ , is [28]:

$$p(f|A, Q_v) = \left( \frac{\det(I - A)^2}{2\pi^{N^2} \det Q_v} \right)^{1/2} \exp \left[ -\frac{1}{2} f^T (I - A)^T Q_v^{-1} (I - A) f \right] \quad (17)$$

By combining Eqs. 16 and 17, dropping all constant terms, multiplying the result by -2 (the maximization problem now becomes minimization due to the sign change), and assuming  $Q_n = \sigma_n^2 I$  and  $Q_v = \sigma_v^2 I$  where  $I$  is the identity matrix, we obtain the following equivalent likelihood function [28]:

$$\hat{\Theta}_{ml} = \arg \left\{ \min_{\Theta \in \Theta} \log(\det P) + g^T P^{-1} s \right\} \quad (18)$$

where  $P$  is the covariance matrix of  $g$  given by:

$$P = \sigma_v^2 H(I - A)^{-1} (I - A)^T H^T + \sigma_n^2 I \quad (19)$$

and  $(\cdot)^{-T}$  and  $(\cdot)^T$  represent inverse transpose, and transpose matrix operations, respectively.

Thus, the problem becomes that of minimizing Eq. 18 with respect to the parameters  $\{h(l,m)\}, \{a(l,m)\}, \sigma_n^2, \sigma_v^2$ . Different implementations exist to solve the nonlinear optimization problem of Eq. 18, such as the gradient-based method, expectation-maximization (EM) technique, prediction error-based technique, and least squares methods. A survey of the different implementations is given in [28]. The EM technique [30] is the most popular because it is straightforward to implement. The method converts the original nonlinear optimization problem of several variables into a linear iterative procedure. The order of the EM implementation is  $O(N_f^2)$ , where  $N_f$  is the total number of pixels in the image estimate. It is a computationally efficient estimation algorithm; however, convergence speed may be slower than for gradient-based methods. Another advantage of this implementation is that an estimate of the true image is produced at every iteration, so the algorithm is easily terminated when a visually appealing result is obtained.

In the next section, we introduce an alternative ARMA estimation algorithm, based on cross-validation. It has higher complexity than ML methods, but is shown to produce better results in simulations.

#### The Generalized Cross-Validation Approach

General cross-validation (GCV) is a widely recognized technique in the field of data analysis. It is sometimes known as “leave-one-out” or predictive sample reuse. Historically, it

has been used as a criterion for estimating the optimal regularization parameter in smoothing problems [58].

The principle behind GCV is straightforward. The data is divided into two sets: an estimation set and a validation set. The estimation set is used to obtain a model or estimate based on a particular parameter value or assumption. The validation set is then used to validate the performance of the model or estimate and thus the assumption. Therefore, many competing parameter values or assumptions may be tested to find the most appropriate. The difficulty with dividing the data into two sets is that it is necessary to use as much of the data as possible to obtain a reliable estimate, but it is also desirable to test the estimate on as much of the data that was excluded from the estimation process as possible. GCV overcomes this problem by allowing all the data to be used for both purposes.

The data is divided into  $M$  sets. The assumption being tested is imposed on all the sets but one, and a validation error measure is computed for the omitted set. The process is repeated, selecting a different set each time, until all the sets have been exhausted. The validation error measures for each set are averaged to produce the validation error for the particular parameter value or assumption. Thus, all the data is used for both estimation and validation.

The GCV technique, when applied to blind image restoration, is straightforward. A “restored” image is estimated using all but one of the from the degraded image  $g$ , for a fixed set of model parameter values. The “restored” image is then reblurred using the selected values for  $h(m,n)$  to predict the observation that was left out of the restoration in the previous step. Different restorations are performed by leaving out a separate pixel of  $g$  each time.

A search technique or optimization method is used to find the parameter set,  $\theta_i$ , which minimizes the mean square prediction error over all the observations (see Table 3). This optimal set is chosen to be the image and PSF model parameter estimates. Table 3 provides a summary of the algorithm. The computational complexity is  $O(N_f^2 N_g)$ , where  $N_f$  and  $N_g$  are the number of pixels of the image estimate, and blurred image, respectively. A computationally simpler algorithm has also been introduced with a slight loss in the quality of restoration [31].

#### *Properties of the ML and GCV Methods*

The advantage of using the ML method to that of the GCV method is that it has a more thoroughly developed history with ARMA modeling. ML parameter estimation is a standard signal processing technique and algorithms such as EM have been developed to make its implementation easier. On the other hand, CV is more robust and has been shown to work better than ML for real images [31].

The ML and GCV methods are less sensitive to additive noise than methods of other classes of blind deconvolution techniques because they take into account the noise in the system. ML methods attempt to estimate the variance of the additive noise,  $\sigma_n^2$ , and GCV methods use the regularization parameter,  $\alpha$ , to reduce noise amplification in the restoration procedure.

**Table 3: Summary of the GCV Algorithm**

**I) Definitions:**

$\theta_i \{ \{h(l,m)\}, \{a(l,m)\}, \alpha \}$ : image, blur, and regularization parameters at the  $i$ th iteration

$\hat{f}_k$ : “restored image,” using all pixels in  $g$  except the  $k$ th pixel

$E^*(\hat{f}, \theta)$ : estimation error

$V(\theta)$ : validation error

$N_g$ : number of pixels in  $g$

**II) Initialization ( $i = 0$ ):**

Set initial values for  $\theta_0 = \{ \{h(l,m)\}, \{a(l,m)\}, \alpha \}$  using a priori information about the PSF or true image, or by inspection of the blurred image.

Set tolerance  $\delta > 0$ .

**III) At iteration ( $i$ ):  $i = 1, 2, \dots, N_g$**

1) If  $i = 0$ , proceed to 2. Otherwise, use the search procedure developed by Powell to update  $\theta_i$  from  $\theta_{i-1}$ .

2) At iteration ( $k$ ):  $k = 0, 1, 2, \dots, N_g$

The following criterion is minimized with respect to  $\hat{f}$  to obtain the “restored image,”  $\hat{f}_k$ . All pixels of  $g$ , but the  $k$ th, are used for the restoration procedure.  $A$  and  $H$  are given from the current value of  $\theta_i$ :

$$E^*(\hat{f}, \theta_i) = \frac{1}{N_g} \sum_{j=1, j \neq k}^{N_g} (g_j - (H\hat{f})_j)^2 + \alpha \| (I - A)\hat{f} \|^p \quad (6)$$

where  $\alpha$  is the regularization parameter used to prevent amplification of noise during the restoration procedure, and the subscript  $j$  denotes the  $j$ th element of the corresponding vector.

3) Using  $\hat{f}_k$  for  $k = 1, 2, \dots, N_g$ , the validation error is calculated to determine how accurate the parameter estimate  $\theta_i$  is. The validation error is given by:

$$V(\theta_i) = \frac{1}{N_g} \sum_{k=1}^{N_g} (g_k - [H\hat{f}_k(\theta_i)]_k)^2 w_{kk}(\theta_i) \quad (7)$$

where  $w_{kk}(\theta_i)$  are weights used to ease the numerical calculation of Eq. 7.

4) If  $\|\theta_i - \theta_{i-1}\| < \delta$ , go to step IV. Otherwise, go to step 1.

IV) If  $\theta_i$  is a good estimate of  $H$ ,  $A$ , and  $[H\hat{f}_k(\theta_i)]_k$ , then should be a good approximation to  $g_k$  averaged over all values of  $k$ . Thus, the parameter set  $\theta_i$ , which produces the minimum value of Eq. 7, is selected as the GCV parameter

A major limitation of these methods is that the log-likelihood function of Eq. 18, and the GCV criterion of the appropriate equation in Table 3 become insensitive to changes in the individual parameters of  $\theta$  when the total number of parameters is large. In addition, there is a chance that the methods may converge to local minima. A hierarchical ML

method has been proposed to reduce the risk of ill-convergence [29]. The ML and CV methods deal only with the second-order signal statistics, so phase cannot be identified uniquely in the restoration procedure unless the PSF is known to be minimum phase. The additional assumptions discussed previously are imposed on the PSF to alleviate such problems. Thus, these ARMA estimation methods are somewhat limited to specific situations.

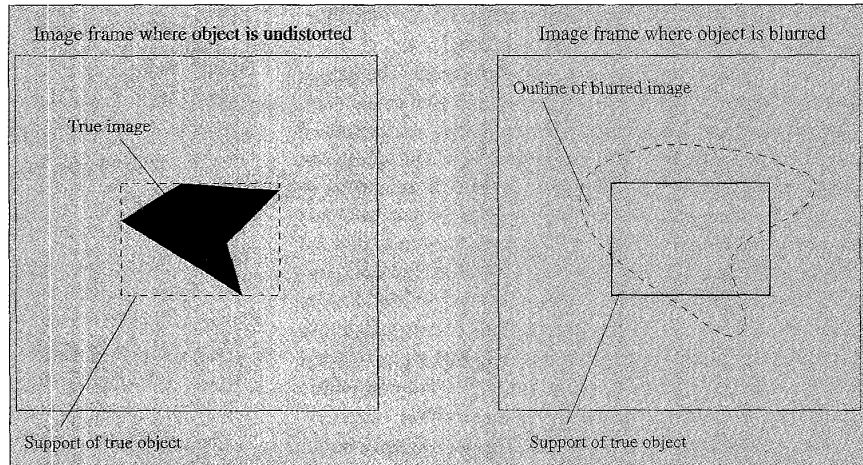
The next class of algorithms do not require that PSF be of minimum phase or that the image have a parametric AR form. Instead, it makes several assumptions on the true image.

### Nonparametric Deterministic Image Constraints Restoration Techniques

In contrast to the methods discussed in the previous sections, the algorithms of this class do not assume parametric models for either the image or the blur. Deterministic constraints such as nonnegativity, known finite support, and existence of blur invariant edges are assumed for the true image. A number of blind deconvolution techniques for images fall into this class, which include the iterative blind deconvolution algorithm [34-39], McCallum's simulated annealing algorithm [40], the nonnegativity and support constraints recursive inverse filtering (NAS-RIF) algorithm [42-44], and the blind superresolution algorithm [45], among others [46].

The methods are iterative and simultaneously estimate the pixels of the true image and the PSF (or its inverse). The constraints on the true image and PSF are incorporated into an optimality criterion which is minimized using numerical techniques.

In this section, we will consider three algorithms: the most well-known method of this class, the iterative blind deconvolution (IBD) algorithm by Ayers and Dainty [34-39]; McCallum's simulated annealing (SA) algorithm [40]; and the nonnegativity and support constraints recursive inverse filtering (NAS-RIF) algorithm [42-44]. With these methods, the true image is assumed to be nonnegative and comprised of an object with known finite support against a uniformly black, grey, or white background. The support refers to the smallest rectangle within which the true object is contained. Thus, the imaging must be performed such that the object is entirely encompassed by the observed frame. This situation often occurs in such diverse applications as astronomical imaging [3], fluorescence microscopy [8], and magnetic resonance imaging [59]. Figure 6 gives an example of a finite support image undistorted and blurred. For situations in which the



6. Example of a finite support image.

support of the true image is unknown, a novel cross-validation-based support finding algorithm proposed in [43] can be used.

Constraints of nonnegativity and support have been used in non-blind restoration problems to improve resolution of gamma-ray spectra [60-61]. Evidence exists that nonnegativity and support information can extrapolate high frequency components lost when the distortion is bandlimiting. Therefore, such constraints hold promise in blind image restoration.

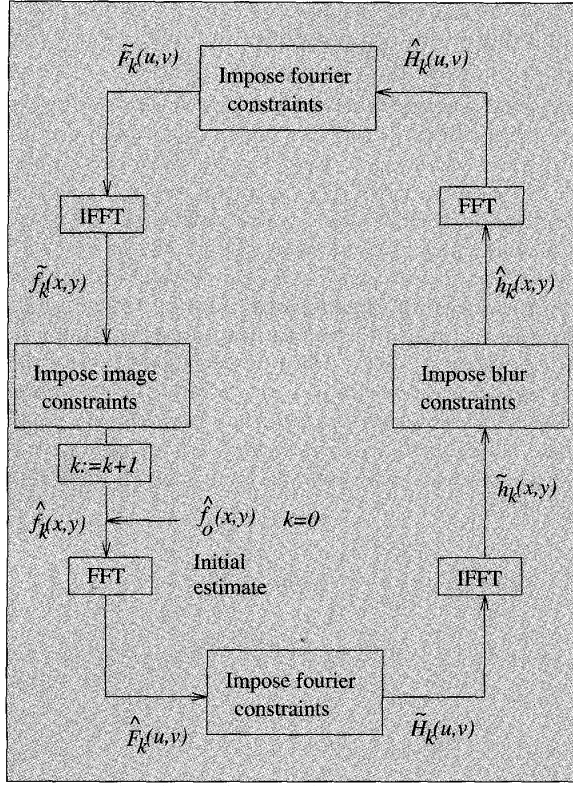
#### *The IBD Method*

The iterative blind deconvolution (IBD) method proposed by Ayers and Dainty is the most popular method in this class. In addition to the assumptions stated above, the method requires that the PSF be nonnegative with known finite support.

The general method makes use of the fast-Fourier transform (FFT) algorithm. The basic structure of the algorithm is presented in Fig. 7. The image estimate is denoted by  $\hat{f}(x,y)$ , the PSF estimate by  $\hat{h}(x,y)$ , and the linearly degraded image by  $g(x,y)$ . The capital letters represent fast-Fourier transformed versions of the corresponding signals. Subscripts denote the iteration number of the algorithm.

After a random initial guess is made for the true image, the algorithm alternates between the image and Fourier domains, enforcing known constraints in each. The constraints are based upon information available about the image and PSF. The image domain constraints can be imposed by replacing negative-valued pixels within the region of support with zero and nonzero pixels outside the region of support with the background pixel value. The Fourier domain constraint involves estimating the PSF (image) using the FFT of the degraded image and image (PSF) estimate. That is, at the  $k$ th iteration,

$$\tilde{H}_k(u,v) = \frac{G(u,v)\hat{F}_{k-1}^*(u,v)}{|\hat{F}_{k-1}(u,v)|^2 + \alpha/|\tilde{H}_{k-1}(u,v)|^2} \quad (20)$$



7. Iterative blind deconvolution method.

$$\tilde{F}_k(u,v) = \frac{G(u,v)\hat{H}_{k-1}^*(u,v)}{|\hat{H}_{k-1}(u,v)|^2 + \alpha/|\hat{F}_{k-1}(u,v)|^2} \quad (21)$$

where  $(\cdot)^*$  denotes the complex conjugate of  $(\cdot)$ . The real constant,  $\alpha$ , represents the energy of the additive noise and is determined by prior knowledge of the noise contamination level, if available. The value of  $\alpha$  must be chosen carefully for reliable restoration. The algorithm is run for a specified number of iterations, or until the estimates begin to converge.

The IBD method is popular for its low computational complexity. Many different implementations of this basic algorithm have been suggested. They differ in their assumptions about the true image and PSF, and how these assumptions are imposed in the image and Fourier domains [34, 35, 37, 38]. Extensions have been proposed for situations in which several degraded versions of the same image are available [36, 39]. Another advantage of this technique is its robustness to noise because of the Wiener-like filters (Eqs. 20 and 21) used in the Fourier domain. Robustness to noise refers to the ability of the algorithm to suppress noise amplification that results from the ill-posed nature of the restoration problem.

The major drawback of the IBD method is its lack of reliability. The uniqueness and convergence properties are, as yet, uncertain. In addition, the restoration is sensitive to the initial image estimate, and the algorithm can exhibit instability.

### The SA Algorithm

McCallum's simulated annealing (SA) algorithm makes the same assumptions on the PSF as the IBD method. It entails the minimization of the following multimodal cost function:

$$J(\hat{f}(x,y), \hat{h}(x,y)) = \sum_{v(x,y)} [\hat{f}(x,y) * \hat{h}(x,y) - g(x,y)]^2 \quad (22)$$

The image and PSF are assumed to be positive with known finite support. Using these constraints on  $\hat{f}(x,y)$  and  $\hat{h}(x,y)$ , a simulated annealing procedure is employed for the minimization of  $J$  with respect to  $\{\hat{f}(x,y)\}$  and  $\{\hat{h}(x,y)\}$ . In simulated annealing [41], estimates of the cost function parameters are iteratively varied to globally minimize  $J$ . The parameter values are randomly perturbed. If the perturbation reduces  $J$ , then it is accepted; if it increases  $J$ , then it is accepted with probability  $p = \exp(-\Delta J/T_k)$ , where  $\Delta J$  is the change in the cost function due to the perturbation, and  $T_k$  is the temperature parameter. As the iterations progress, the temperature parameter  $T_k$  is reduced (i.e.,  $p$  is reduced). Simulated annealing optimization is analogous to the annealing of metals.

When liquid metal is cooled (i.e., the temperature is reduced) sufficiently slowly, it reaches the absolute minimum energy state related to complete atomic ordering of the metal. If the liquid is cooled too quickly, then the atoms reach a suboptimal energy state. Similarly, in simulated annealing, the temperature parameter  $T_k$  must be reduced "slowly" every iteration to reach the global minimum of  $J$ , otherwise it may reach a local minimum. In the case of infinite precision and infinitely many iterations, the minimization procedure is guaranteed to reach the global minimum of a multimodal cost function.

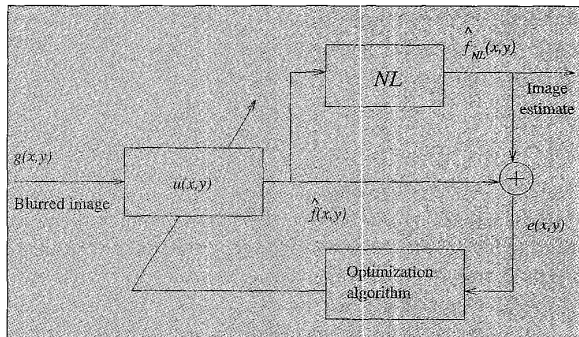
The SA algorithm for blind image restoration is given in Table 4. The algorithm is reliable and provides reasonable results in the presence of noise. The major disadvantage is that convergence to the global minimum of the cost function is slow. The speed of convergence of the algorithm depends to a large extent on how quickly  $T_k$  is reduced. For realistically sized images, the algorithm is too computationally intensive to produce a good solution.

### The NAS-RIF Algorithm

The nonnegativity and support constraints recursive inverse filtering (NAS-RIF) algorithm was introduced to overcome the problems associated with the poor convergence properties of the IBD method and the high computational complexity of the SA method. This method makes the same assumptions on the true image as the IBD and SA methods. The only assumptions made on the PSF, however, is that it is absolutely summable, that is,  $\sum_v(x,y) |h(x,y)| < \infty$ , and that it has an inverse  $h^{-1}(x,y)$  that is also absolutely summable. No other constraints are imposed on the PSF. An advantage of this method is that it does not require the PSF to be of known finite extent, as do the other methods; this information is often difficult to obtain.

**Table 4: Summary of McCallum's Simulated Annealing Algorithm**

<b>I) Definitions:</b>
$f(x,y)$ : image estimate
$\hat{h}(x,y)$ : PSF estimate
$T_k$ : temperature parameter
$MaxCycle$ : maximum number of cycles for algorithm
$MaxScan$ : maximum number of scans per cycle
<b>II) Set initial conditions (<math>k = \emptyset, j = 0</math>):</b>
Randomly initialize $\hat{f}(x,y)$ and $\hat{h}(x,y)$
Set temperature parameter $T_k > 0$
Set $MaxCycle \in \mathbb{N}$
Set $MaxScan \in \mathbb{N}$
<b>III) At cycle (<math>k</math>): <math>k = 0, 1, 2, \dots, MaxCycle</math></b>
$T_k = 0.8T_i, \lambda_k = 100\sqrt{T_k}$
Scale $\hat{f}(x,y)$ and $\hat{h}(x,y)$ to have the same rms values, keeping $g$ the energy of $\hat{f}(x,y) * \hat{h}(x,y)$ constant.
At scan ( $j$ ): $j = 0, 1, 2, \dots, MaxScan$
1) For every image estimate pixel, perturb the pixel by a random quantity proportional to $\lambda_k$ . If the following cost decreases, accept the change, otherwise accept with probability $\exp(-\Delta/T_k)$ where $\Delta$ is the increase in cost due to the perturbation. The cost $J$ is given by:
$J = \sum_{(x,y) \in \gamma_f} \hat{f}^2(x,y) + \sum_{(x,y) \in \gamma_h} \hat{h}^2(x,y) + \sum_{(x,y) \in \gamma_g} [g(x,y) - \hat{h}(x,y) * \hat{f}(x,y)]^2$
where $\gamma_f, \gamma_h$ are the set of pixel locations deviating from the known constraints of nonnegativity and support for the true image and true PSF, respectively.



8. NAS-RIF algorithm.

The NAS-RIF technique is shown in Fig. 8. It consists of a variable FIR filter  $u(x,y)$  with the blurred image  $g(x,y)$  as input. The output of this filter represents an estimate of the true image  $\hat{f}(x,y)$ . This estimate is passed through a nonlinear filter, which uses a non-expansive mapping to project the

estimated image into the space representing the known characteristics of the true image. The difference between the projected image  $\hat{f}_{NL}(x,y)$  and  $\hat{f}(x,y)$  is used as the error signal to update the variable filter  $u(x,y)$ . In general, a variety of image constraints may be imposed in the nonlinear filter denoted by  $NL$  in Fig. 8. Table 5 gives a list of possibilities.

If we assume the image is nonnegative with known support, the  $NL$  block of Fig. 8 represents the projection of the estimated image onto the set of images that are nonnegative with given finite support. Thus, the negative pixel values within the region of support must be zero, and the pixel values outside the region of support are the background grey-level,  $L_B$ , as shown in Table 5. Either the nonnegativity constraint or support constraint or both can be used for restoration. Experience shows that the support information is more useful than nonnegativity, which often yields ambiguous non-unique solutions. The cost function for this particular situation is:

$$\begin{aligned} J(u) &= \sum_{v(x,y)} e^2(x,y) + \gamma \left[ \sum_{v(x,y)} u(s,y) - 1 \right]^2 \\ &= \sum_{(x,y) \in D_{sup}} \hat{f}^2(x,y) \left[ \frac{1 - \text{sgn}(\hat{f}(x,y))}{2} \right] \\ &\quad + \sum_{(x,y) \in \bar{D}_{sup}} [\hat{f}(x,y) - L_B]^2 + \gamma \left[ \sum_{v(x,y)} u(x,y) - 1 \right]^2 \end{aligned} \quad (23, 24)$$

where  $\hat{f}(x,y) = g(x,y) * u(x,y)$ ,  $D_{sup}$  is the set of all pixels inside the region of support, and  $\bar{D}_{sup}$  is the set of all pixels outside the region of support. The variable  $\gamma$  in the third term of Eq. 24 is nonzero only when  $L_B$  is zero, i.e., the background color is black. The third term is used to constrain the parameters away from the trivial all-zero global minimum for this situation [42].

It can be shown that Eq. 24 is convex with respect to  $u(x,y)$ , so that convergence of the algorithm to the global minimum is possible using a variety of numerical optimization routines. The conjugate gradient minimization routine was used for minimization of  $J$  in [42-44] because its speed of convergence is much faster than other descent routines, such as the steepest-descent method. Table 6 provides the method in basic algorithmic form.

#### Comparing the IBD, SA, and NAS-RIF Algorithms

This section provides a comparison of the performance of the methods in this class based on convergence, computational complexity, and sensitivity to noise. The NAS-RIF algorithm is guaranteed to converge to the feasible set of solutions because it deals with the minimization of a convex cost function. The algorithm is well-behaved and stable, unlike the IBD algorithm. In addition, the NAS-RIF algorithm converges faster for large images.

The convergence properties of the IBD algorithm are sensitive to the initial conditions and the noise parameter  $\alpha$ , as shown in Eqs. 20-21. Although the SA method guarantees convergence to the global minimum in an infinite number of

**Table 5: Possible Implementations of the NL Filter for the NAS-RIF Method**

Constraint	Nonlinear (NL) Filter
Nonnegativity	$\hat{f}_{NL}(x,y) = \begin{cases} \hat{f}(x,y) & \text{if } \hat{f}(x,y) \geq 0 \\ 0 & \text{otherwise} \end{cases}$
Finite Support denoted by $D_{sup}$ ; where $L_B$ is the background pixel color	$\hat{f}_{NL}(x,y) = \begin{cases} \hat{f}(x,y) & \text{if } (x,y) \in D_{sup} \\ L_B & \text{otherwise} \end{cases}$
Bounds on pixel amplitude $m_f \leq f(x,y) \leq M_f$	$\hat{f}_{NL}(x,y) = \begin{cases} m_f & \text{if } \hat{f}(x,y) < m_f \\ M_f & \text{if } \hat{f}(x,y) > M_f \\ \hat{f}(x,y) & \text{otherwise} \end{cases}$
Nonnegativity and Maximum Energy Constraint $\sum_{(x,y)} f^2(x,y) \leq E$	$\hat{f}_{NL}(x,y) = \begin{cases} 0 & \text{if } \hat{f}(x,y) < 0 \\ \hat{f}(x,y) & \text{if } \hat{E} \leq E \\ \sqrt{\frac{E}{\hat{E}}} \hat{f}(x,y) & \text{otherwise} \end{cases}$ where $\hat{E}$ is the energy of $\hat{f}(x,y)$
Smoothness Constraint: pixels in the region $D_{smooth}$ are considered to be smooth	$\hat{f}_{NL}(x,y) = \begin{cases} \hat{f}(x,y) & \text{if } \hat{f}(x,y) \in D_{smooth} \\ + \sum_{(m,n) \in S} \hat{f}(m,n) & \text{otherwise} \end{cases}$ where $S$ is some rectangular window of pixels centered at $(x,y)$ , and $N$ is the total number of elements of $S$

iterations and with infinite precision, the algorithm is too computationally complex to be feasible for real imaging applications; the order of the algorithm per iteration is  $O(N_f^4)$ , where  $N_f$  the number of pixel values of the image estimate.

In contrast, the IBD method has order  $O(N_f \log_2(N_f))$ , and the NAS-RIF method has order  $O(N_f N_u N_{ls,k})$  per iteration, where  $N_u$  is the number of FIR filter parameters of  $u(x,y)$ , and  $N_{ls,k}$  is the number of line searches required at the  $k$ th iteration. Since the number of filter parameters is usually much smaller than the image size, the NAS-RIF method requires fewer computations, on average, than the IBD method to produce a good estimate.

The main advantage of the IBD method over the NAS-RIF algorithm is that it incorporates a Wiener-like filter into the restoration process. This filter largely prevents noise amplification from occurring. The NAS-RIF algorithm shows some noise amplification at low SNRs, but premature termination of the algorithm may be employed to prevent this [44].

#### Nonparametric Methods Based on High Order Statistics

This class of techniques is structurally similar to the NAS-RIF algorithm, and is useful for restoring texture images [18, 47-48]. They are based on minimizing the given cost function that accounts for the probabilistic non-Gaussian nature of the true image. The degraded image is passed through an FIR inverse filter, yielding an estimate of the true image. The FIR filter parameters are updated in order to optimize a function

that incorporates the high order statistics (HOS) model of the true image. Figure 9 provides an overview of the scheme.

A well-known technique in this class is minimum entropy deconvolution (MED) [18], which attempts to find the FIR inverse filter of the PSF that yields the smallest output entropy when applied to the degraded image. This technique maximizes the simple “spike-like” character of the true image estimate. This is useful for applications like astronomy, in which the true image is composed of bright spots against a dark background; and geophysics, where teleseismic signals have a spike-like nature. MED has also been proposed for restoring two-tone images [47]. The general algorithm is provided in Table 7.

The various algorithms of this class differ in their choice of  $g(\cdot)$ , shown in Table 7. For MED [18], the function  $g[f] = f^3$  is used. For Bayesian non-minimum phase approaches [48],  $g(\cdot)$  is used to reshape the marginal pdf of the signal  $\hat{f}_k(x,y)$  to be that of the true image, and is derived for the particular pdf.

The algorithm is an extension of the Bussgang class of algorithms for communication channels [52]. The technique has structural similarities to the NAS-RIF algorithm, but is applicable only for situations in which the true image can be represented as a known stationary stochastic signal.

The main advantages of methods in this class is that they can identify non-minimum phase PSFs, and are fairly robust to noise. The primary limitations are that the true image must be accurately modeled by a known non-Gaussian probability

Table 6: Summary of the NAS-RIF Algorithm

**I) Definitions:**

- $f_k(x,y)$ : estimate of true image
- $u_k(x,y)$ : FIR filter parameters of dimension  $N_{xu} \times N_{yu}$  at iteration  $k$
- $g(x,y)$ : blurred image
- $\delta$ : tolerance used to terminate algorithm
- $J(u_k)$ : cost function at parameter setting  $u_k$
- $\nabla J(u_k)$ : gradient of  $J$  at  $u_k$
- $\langle \cdot, \cdot \rangle$ : scalar product

Note: bold letters represent lexicographically ordered vectors of their two-dimensional counterparts.

**II) Set initial conditions ( $k = 0$ ):**

- Set FIR filter  $u_0(x,y)$  to all zeros with a unit spike in the middle
- Set tolerance  $\delta > 0$

**III) At iteration ( $k$ ):  $k = 0, 1, 2, \dots$**

- 1)  $\hat{f}_k(x,y) = u_k(x,y)^* g(x,y)$
- 2)  $\hat{f}_{N_u}(x,y) = NL[\hat{f}(x,y)]$
- 3) Minimization Routine to update FIR filter parameters.

For example, (conjugate gradient routine)

$$3a) [\nabla J(u_k)]^T = \left[ \frac{\partial J(u_k)}{\partial u(1,1)} \frac{\partial J(u_k)}{\partial u(1,2)} \cdots \frac{\partial J(u_k)}{\partial u(N_{xu}, N_{yu})} \right] \text{ where}$$

$$\frac{\partial J(u_k)}{\partial u(i,j)} = 2 \sum_{(x,y) \in D_{\text{spp}}} \hat{f}_k(x,y) \left[ \frac{1 - \text{sgn}(\hat{f}_k(x,y))}{2} \right] g(x-i+1, y-j+1)$$

$$+ 2 \sum_{(x,y) \in D_{\text{spp}}} [\hat{f}_k(x,y) - L_B] g(x-i+1, y-j+1) + 2 \gamma \left[ \sum_{(x,y)} u_k(x,y) - 1 \right]$$

$$3b) \beta_{k,l} = (\langle -\nabla J(u_k) - \nabla J(u_{k,l}), \nabla J(u_k) \rangle / \langle -\nabla J(u_{k,l}), \nabla J(u_{k,l}) \rangle)^{1/2}$$

$$3c) \text{If } k = 0, d_k = -\nabla J(u_k). \text{ Otherwise, } d_k = -\nabla J(u_k) + \beta_{k,l} d_{k,l}$$

$$3d) \text{Perform a line minimization such as } \text{dlinmin}, \mathbf{c} \text{ to find } t_k \text{ such that } J(u_k + t_k d_k) \leq J(u_k + t d_k) \text{ for all } t \in \mathbb{R}$$

$$3e) u_{k+l} = u_k + t_k d_k$$

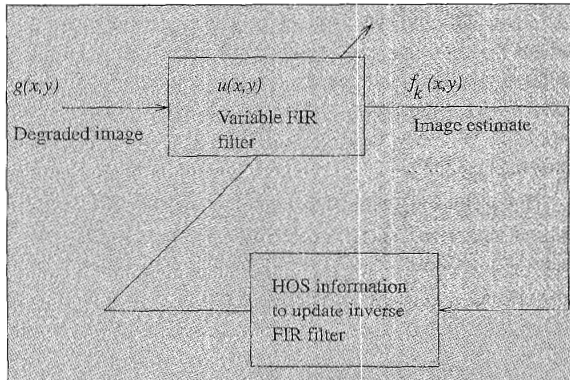
$$4) k = k + 1$$

$$5) \text{If } J(u_k) < \delta, \text{ stop. Otherwise, go to 1.}$$

## Simulation Examples

A variety of different methods exist for blind deconvolution of images with varying assumptions on the true image and PSF. For the purpose of comparison, these assumptions are controlled in the simulations. In this section, we compare the performance of methods of the same class, i.e., nonparametric deterministic image constraints methods. These methods have been selected for simulation as they are a more general class of techniques and are portable to many different applications. They also have moderate to low computational requirements, which makes them more practical for real imaging situations.

The simulations are provided to give an idea of the ability of blind deconvolution. Examples of the performance of the other methods discussed can be found with the corresponding authors. Simulations were conducted for the case of images with a black ( $L_B = 0$ ) background. Some test images were synthetically degraded by convolving the true image with an artificially generated PSF, and then adding a zero-mean Gaussian noise realization. Restorations of real image data are also provided later.



9. Basic scheme for methods based on high order statistics.

distribution, and the algorithms may become trapped in local minima. The computational complexity of this class of methods is  $O(N_f^2 + N_f N_u)$ , where  $N_f$  is the number of pixels in the image estimate, and  $N_u$  is the number of parameters in the variable FIR filter,  $u(x,y)$ .

**Table 7: Summary of the HOS-based Methods**

- I) Definitions:**
  - $f_k(x,y)$  : estimate of the true image at the  $k$ th iteration
  - $u_k(x,y)$  : FIR inverse filter at the  $k$ th iteration
  - $g(z,y)$  : degraded image
  - $R_{gg}$  : covariance matrix of  $g(z,y)$  given by  $E\{gg^T\}$
  - $R_{gfNLk}$  : cross-covariance matrix between  $g(z,y)$  and  $f_k(x,y)$
  - $g[\cdot]$ : zero-memory nonlinearity
  - Note: Bold letters represent lexicographically ordered version of their two-dimensional counterparts.
- II) Initialize variables ( $k = 0$ ):**
  - Inverse filter:  $u_k(x,y)$  is composed of all zeros with a unit spike in the middle.
- III) At iteration ( $k$ ):  $k = 0, 1, 2, \dots$** 
  - 1)  $\hat{f}_k(x,y) = u_k(x,y) * g(x,y)$
  - 2)  $\hat{f}_{NL,k} = g[\hat{f}_k]$
  - 3)  $u_k = R_g^{-1} R_{g\hat{f}} f_{NL,k}$
  - 4)  $k = k + 1$
  - 5) If  $u_k$  stabilizes, stop. Otherwise, go to 1.

The following acronyms are used to refer to the different techniques:

**IBD:** Iterative Blind Deconvolution method

**SA:** Simulated Annealing algorithm

**NAS-RIF:** Nonnegativity and Support constraints Recursive Inverse Filtering algorithm

The IBD, SA, and NAS-RIF algorithms have been previously described. These methods are compared on the basis of their convergence properties, performance under high SNR conditions, performance under moderate SNR conditions, and performance when the support size is incorrect.

Two related measures of performance will be used to help assess the quality of the restorations: the percentage mean square error (MSE), and the improvement in signal-to-noise ratio (SNRI). These quantities are defined below:

$$MSE(\hat{f}) \triangleq 100 \frac{\sum_{\forall(x,y)} [a\hat{f}(x,y) - f(x,y)]^2}{\sum_{\forall(x,y)} f^2(x,y)} \quad (25)$$

$$SNRI \triangleq \frac{MSE(g)}{MSE(\hat{f})} \quad (26)$$

Because any scaled version of the image estimate is desired,  $a$  is chosen such that  $MSE(\hat{f})$  is minimized. Specifically,

$$a = \frac{\sum_{\forall(x,y)} f(x,y)\hat{f}(x,y)}{\sum_{\forall(x,y)} \hat{f}^2(x,y)} \quad (27)$$

The problem of obtaining a shifted version of the image is not considered in the MSE calculation, since one of the constraints applied on the true image in these algorithms is finite known support that is kept in a fixed location. Thus, no shifting occurs between subsequent iterations of the restoration algorithms. Even though the MSE is not a reliable estimator of the subjective quality of a restored image, it will be used to give some indication of the performance of the schemes.

The results for the following synthetically blurred images are presented:

**BIR image:** a synthetically generated binary text image of the words “BLIND IMAGE RESTORATION”

**toy image:** a grey-scale image of a toy

**UT image:** a synthetically generated binary image of the letters “UT”

Each of these test images were synthetically blurred using the linear degraded model of Eq. 4, with one of three types of PSFs, referred to by their dimensions. A brief description of each PSF is provided below. Figure 10 displays the PSFs (negative pixels are displayed as black).

**23 x 23 PSF:** a separable PSF generated from  $\psi\psi^T$ , where  $\psi$  is a column vector geometrically decreasing from the center by a factor of 0.7.

**21 x 21 PSF:** a radially symmetric PSF, geometrically decreasing from the center by a factor of 0.8. This type of PSF is often found in applications like x-ray imaging and astronomy.

**5 x 5 PSF:** a separable PSF, linearly decreasing in amplitude from the center.

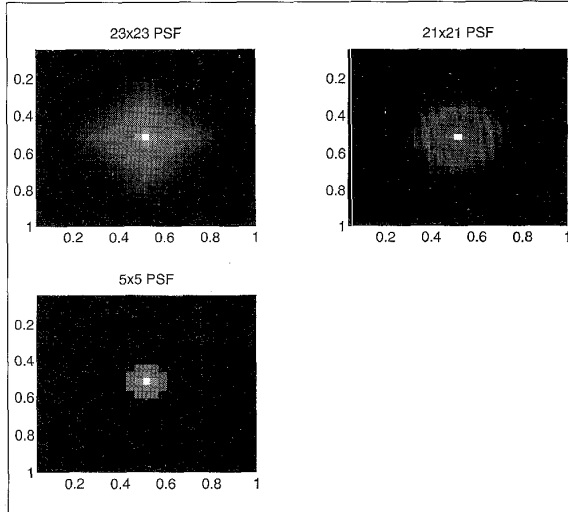
### Performance under High SNR Conditions

This section discusses the performance of the algorithms for high signal-to-noise (SNR) conditions. The performance of the algorithms is similar to that for ideal noiseless conditions. The following results are obtained for an SNR of 70 dB in all cases.

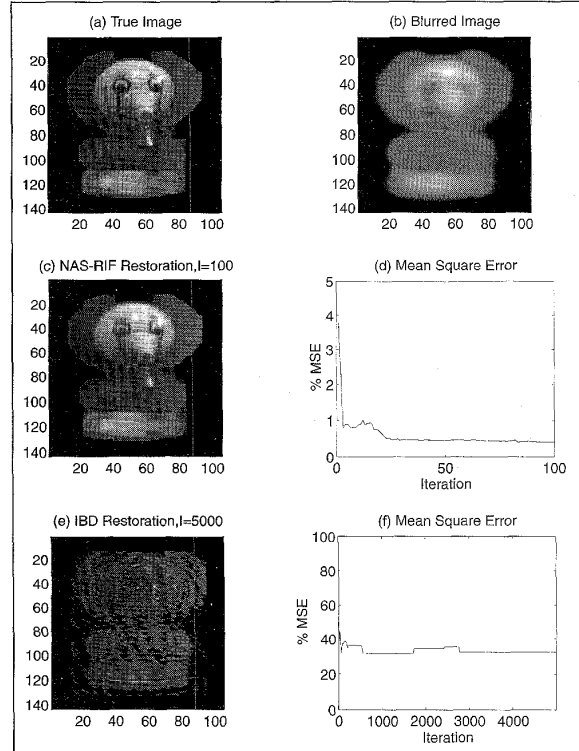
Figure 11 shows the results for the BIR image with the 23 x 23 PSF. The IBD method takes approximately an order of magnitude longer to converge than the NAS-RIF method, as shown in the MSE plots of Figs. 11d and 11f. The SA method was too computationally complex to produce a solution for an image of this size.

Figure 12 shows the results for the toy image with the 23 x 23 PSF. The NAS-RIF algorithm converges to a good solution within 100 iterations. The IBD algorithm was run for 5000 iterations and was unable to converge to a good solution. Many different initial conditions and noise parameter ( $\alpha$ ) values were simulated, but the algorithm did not converge properly for any of them.

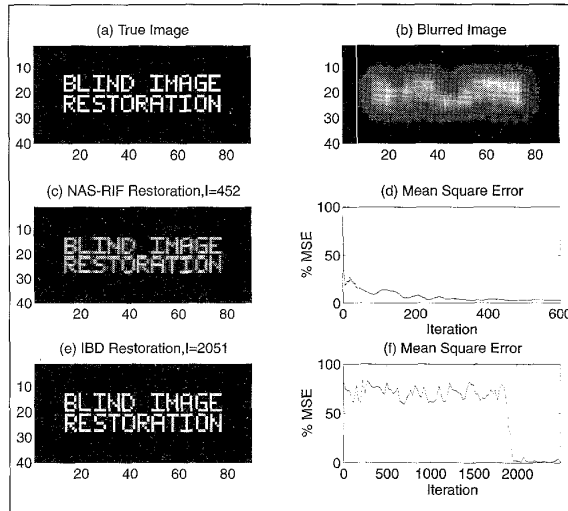
The results of the algorithms are shown in Fig. 13 for the UT image blurred by the 5 x 5 PSF. The NAS-RIF algorithm converges in the fewest number of iterations. One must note



10. Synthetic test PSFs used for simulations.



12. Results for the toy image degraded by the  $23 \times 23$  PSF for an SNR of 70 dB.



11. Results for the BIR image degraded by the  $23 \times 23$  PSF for an SNR of 70 dB.

that the SA method converges in 40 cycles. The algorithm has 50 scans per cycle, so that this is equivalent to 2000 iterations, which is greater than that required by the IBD algorithm.

For high SNRs, the NAS-RIF algorithm shows the most desirable convergence properties of the three algorithms. The IBD algorithm does not converge for complicated grey-scale images, and the SA method is too computationally complex.

#### Performance under Moderate SNR Conditions

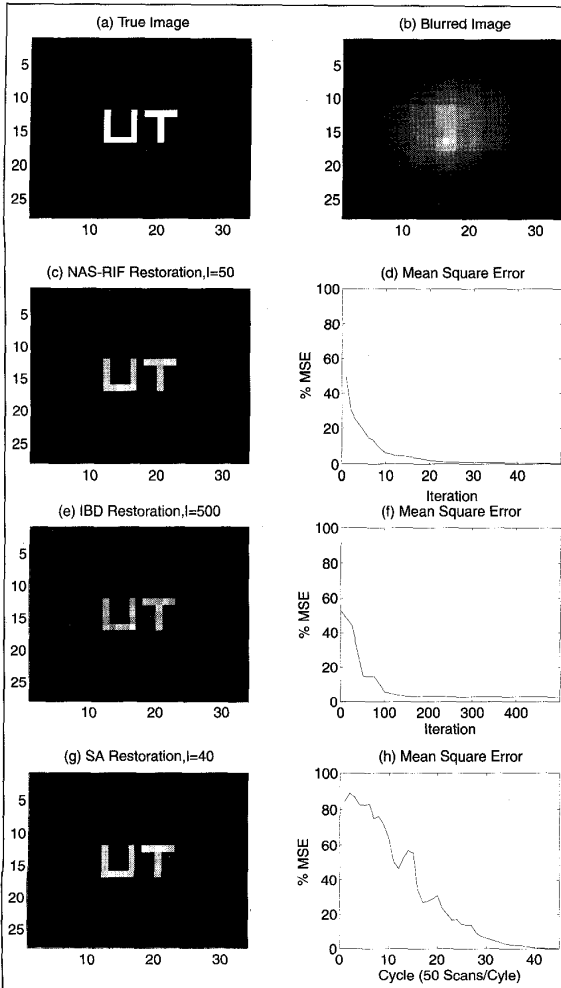
This section examines the behavior of the methods for lower SNRs. Simulation results are presented for the three algorithms at an SNR of 50 dB. The IBD algorithm is the most robust to noise; the NAS-RIF method is the most sensitive.

Simulations for the BIR image blurred by the  $21 \times 21$  PSF were conducted using 10 independent noise realizations. The results are displayed in Fig. 14. The best and worst restorations, and the average of the 10 restorations are shown. Although the best and average restorations are comparable for the IBD and NAS-RIF methods, the worst NAS-RIF restoration shows noise amplification. The MSEs of the two methods are shown in Fig 14g and 14h. The solid lines are the MSEs for the best restorations and the dashed lines are for the worst restorations. From Fig. 14g, it is apparent that the NAS-RIF algorithm begins to converge to a good solution, but then exhibits noise amplification on subsequent iterations. Therefore, it is possible to monitor the algorithm and prematurely terminate it when a visually appealing result is obtained.

#### Performance for Inaccurate Support Size

This section discusses the behavior of the algorithms for inaccurate support. The three algorithms did not converge to an acceptable solution for underestimated supports. In fact, the IBD method showed instability.

For overestimated supports, the IBD method experienced difficulty in converging to a solution. However, The NAS-RIF method was highly robust to the overestimation. Figure 15 shows the results of the NAS-RIF algorithm for the BIR image and  $21 \times 21$  PSF for incorrect supports. The BIR image has an actual support of  $15 \times 65$ . The NAS-RIF algorithm



13. Results for the UT image degraded by the  $23 \times 23$  PSF for an SNR of 70 dB.

assuming incorrect supports of  $17 \times 67$  and  $13 \times 63$  was simulated.

#### Results for Real Image Data

In this section, we provide the restoration results of the NAS-RIF and IBD algorithms on the “j413\_crr.fit” image of Jupiter taken by the Hubble Space Telescope (HST). The data was prepared by STScI, and can be found in the **software/stsdas/restore** directory at the stsci.edu internet site.

The degraded Hubble data is shown in Fig. 16a. A non-blind restoration using the Adaptive Regularized Restoration algorithm by Katsaggelos, *et al.* [65] is shown in Fig. 16b. This algorithm requires knowledge of the PSF in the restoration process. The non-blind restoration is used to provide a basis of visual evaluation of the performance of the blind deconvolution methods. The data displayed in Figs. 16a and 16b were taken with permission from [65].

The IBD and NAS-RIF restorations are displayed in Figs. 16h for an estimated support size  $282 \times 294$ . Fig. 16c gives

the IBD restoration. The algorithm was run for over 2500 iterations. The estimate that showed the minimum mean squared error from the known nonnegativity and support constraints is taken to be the “best” image estimate.

Figure 16e gives the NAS-RIF restoration for a FIR filter length of  $7 \times 7$  and, similarly, Fig. 16g for a filter length of  $25 \times 25$ . As the filter length is increased, there is improved clarity in the restoration. A possibility for the higher variance of the image in Fig. 16e is the coarse, four-bit quantization of the original degraded image. The authors believe that the smoother appearance of the non-blind restoration in Fig. 16b is due to the regularization method incorporated in the algorithm.

The absolute mean deviation (AMD) for each of the restorations with respect to the blurred image is given in Table 8. The AMD is defined as

$$AMD(\hat{f}) = \frac{\sum_{\forall(x,y)} |g(x,y) - bf(x,y)|}{\sum_{\forall(x,y)} |g(x,y)|}$$

where

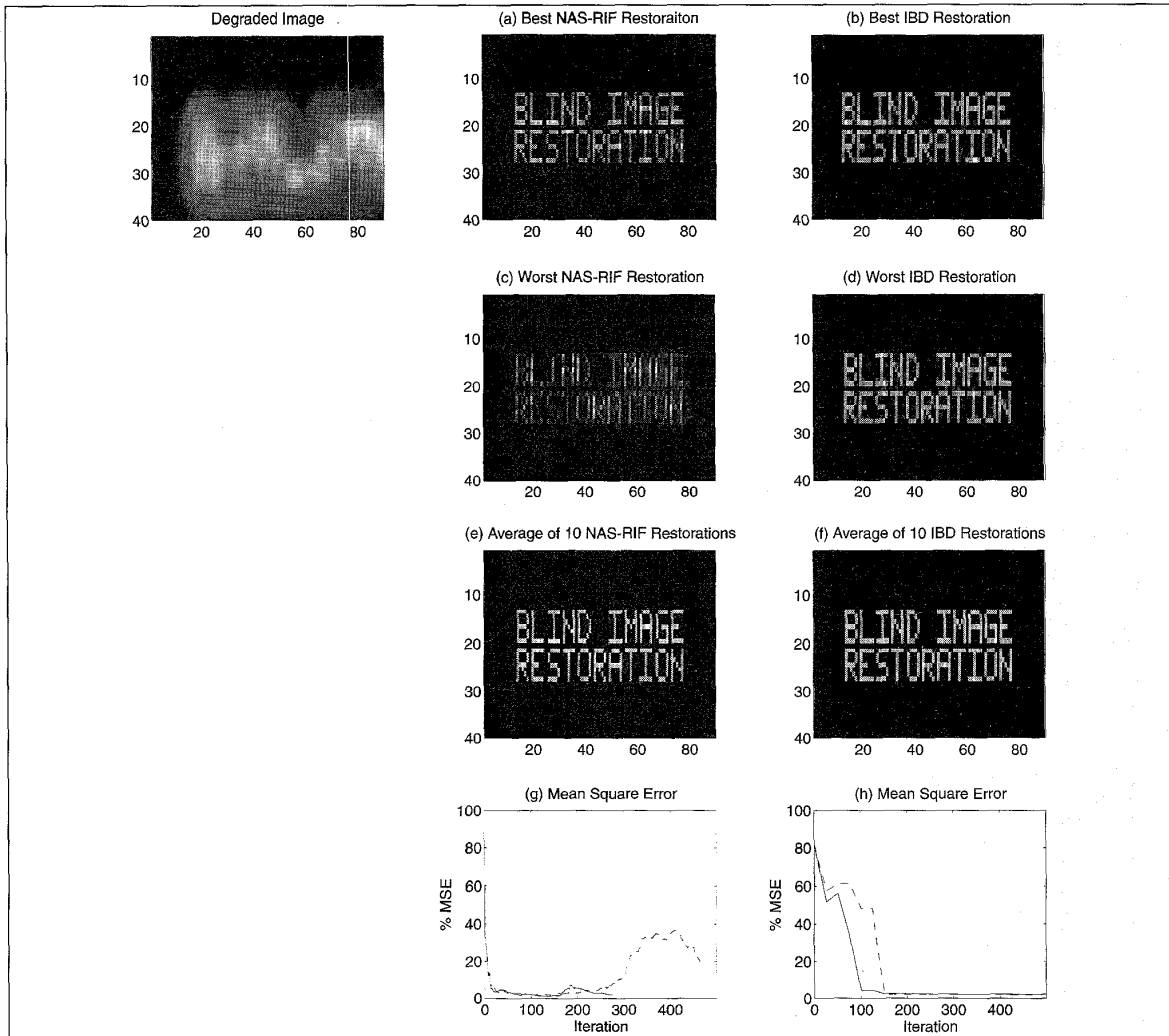
$$b = \frac{\sum_{\forall(x,y)} g(x,y)}{\sum_{\forall(x,y)} f(x,y)}$$

Table 8 gives the AMDs of the restored images of Jupiter. The AMD provides, to some extent, a measure of the amount of “deblurring” by the corresponding restoration algorithm. The AMDs for the non-blind restoration and the NAS-RIF method using a  $25 \times 25$  filter are the closest in magnitude. This indicates, in some sense, a similarity in the restorations. Visual inspection of Figs 16b and 16g also demonstrates the similarities of the two estimates. Thus, blind deconvolution algorithms are useful tools for improving the quality of real blurred images.

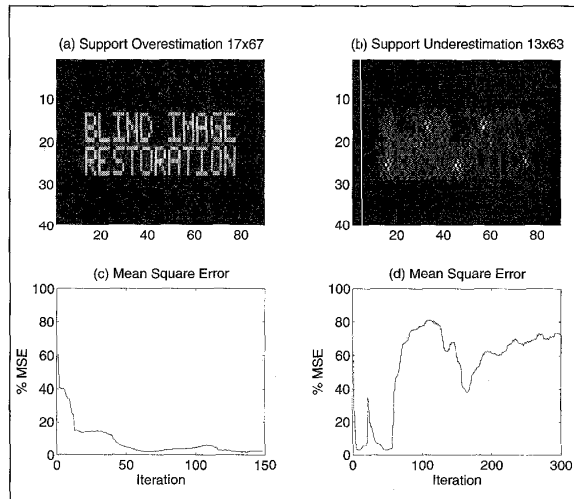
#### Summary and Conclusions

This article provided an overview of the major approaches to the problem of blind deconvolution of images. Algorithms can be grouped into the five major classes, and well-known algorithms of each class have been described. Table 9 provides a summary of the general characteristics of the various approaches. The classification provides an idea of the average, not individual, behavior of the algorithms in each approach.

The need for more practical image restoration algorithms in situations where partial information is available about the true image, and PSF has sparked research in the area of blind deconvolution. Although many approaches for solving the problem have been proposed for different applications (including methods which do not fall under the the five classes [49-51]), there is still a need for developing techniques that exhibit a more appropriate compromise among computational complexity, convergence properties, portability, and reliability for a given application.



14. Results for the BIR image degraded by the  $21 \times 21$  PSF at a BSNR of 50 dB.



15. NAS-RAF algorithm results for inaccurate support sizes.

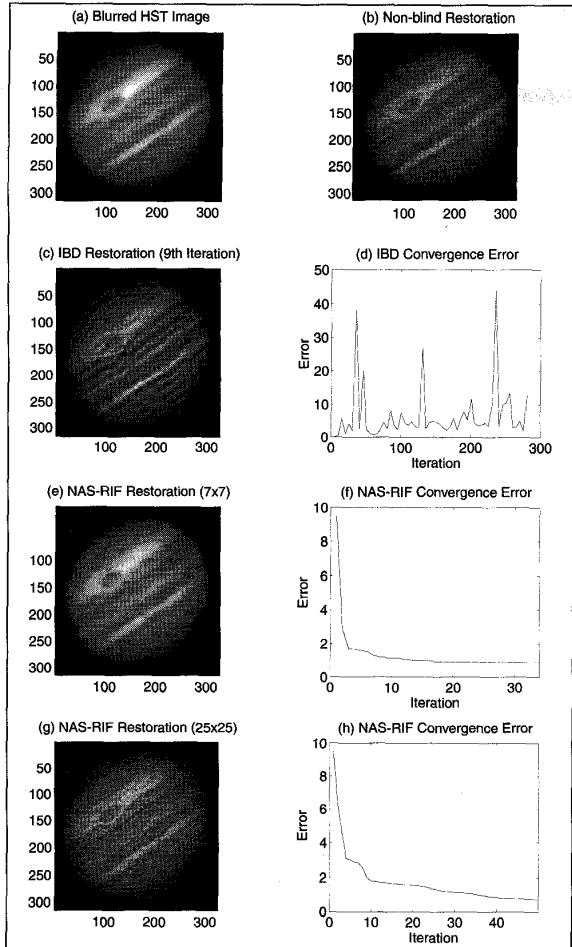
## Acknowledgment

The authors wish to acknowledge Professor A. Katsaggelos for some of the simulation results included in this work, and the Natural Sciences and Engineering Research Council for funding this research.

Deepa Kundur is a Ph.D. candidate, and Dimitrios Hatzinakos Professor of Electrical Engineering, in the Department of Electrical and Computer Engineering, University of Toronto, Ontario, Canada.

## Bibliography

1. A. K. Katsaggelos, ed., *Digital Image Restoration*. New York: Springer-Verlag, 1991.
2. H. C. Andrews and B. R. Hunt, *Digital Image Restoration*. New Jersey: Prentice-Hall, Inc., 1977.



16. (a) Real HST data, (b) non-blind adaptive regularized restoration, (c) IBD restoration (best estimate achieved for 9th iteration), (d) IBD convergence error, (e) NAS-RIF restoration for a filter length of  $7 \times 7$ , (f) NAS-RIF convergence error associated with restoration in (e), (g) NAS-RIF Restoration for a FIR filter length of  $25 \times 25$ , (h) NAS-RIF convergence error associated with restoration in (g). Images in (a) and (b) were obtained from Kataggelos et. al [65] with permission.

**Table 8: Absolute Mean Deviation of the Restorations**

Restoration Method	AMD w.r.t. Blurred Image
Non-blind restoration	0.1197
NAS-RIF ( $7 \times 7$ filter)	0.0353
NAS-RIF ( $25 \times 25$ filter)	0.1020
IBD	0.1599

3. R. H. T. Bates, "Astronomical speckle imaging," *Phys Rep.*, vol. 90(4), pp. 203-97, Oct. 1982.  
 4. J. P. Muller, ed., *Digital Image Processing in Remote Sensing*, pp. 226-269, Philadelphia: Taylor & Francis, 1988.

5. K. Faulkner, C. J. Kotre and M. Louka, "Veiling glare deconvolution of images produced by x-ray image intensifiers," *Third Int Conf on Image Proc and Its Applications*, pp. 669-673, July 1989.

6. T. Wilson and S. J. Hewlett, "Imaging strategies in three-dimensional confocal microscopy," *Biomedical Image Processing*, Alan C. Bovik, William E. Higgins, Eds., Proc. SPIE 1245, pp. 35-45, 1991.

7. S. N. Drossos, "Fast artifact free reconstruction algorithm for limited data (PET) using constrained optimization," *Third International Conference on Image Processing and Its Applications*, pp. 367-372, July 1989.

8. V. Krishnamurthi, Yi-Hwa Liu, Timothy J. Holmes, "Blind deconvolution of 2D and 3D fluorescent micrographs," *Biomedical Image Processing and Three-Dimensional Microscopy*, Raj S. Acharya, Carol J. Cogswell, Dmitry B. Goldgof, Eds., Proc. SPIE 1660, pp. 95-102, 1992.

9. A. K. Jain and S. Ranganath, "Applications of two dimensional spectral estimation in image restoration," *Proc IEEE Int Conf Acoustics, Speech, Signal Processing*, pp. 1113-1116, 1981.

10. B. R. Hunt, "The application of constrained least squares estimation to image restoration by digital computer," *IEEE Trans Comput*, C-22, pp. 805-812, Sept. 1973.

11. A. O. Aboutalib and L. M. Silverman, "Restoration of motion degraded images," *IEEE Trans Cir Sys*, CAS-22, pp. 278-286, March 1975.

12. J. Biemond, R. L. Lagendijk, and R. M. Mersereau, "Iterative methods for image deblurring," *Proc IEEE*, vol. 78(5), pp. 856-883, May 1990.

13. T. J. Schulz, "Multiframe blind deconvolution of astronomical images," *J Opt Soc Am A*, vol. 10(5), pp. 1064-1073, May 1993.

14. M. J. B. Crowther and M. C. Fernandez, "Imaging in videoconferencing now: telemedicine in Somalia," *Advanced Imaging*, pp. 28-31, Oct. 1993.

15. A. G. Qureshi and H. T. Mouftah, "Partially-blind image restoration using constrained Kalman filtering," *Proc IEEE Int Conf Acoustics, Speech, Signal Processing*, pp. 3713-3716, 1991.

16. P. Nisenson and R. Barakat, "Partial atmospheric correction with adaptive optics," *J Opt Soc Am A*, vol. 4, pp. 2249-2253, 1991.

17. M. C. Roggemann, "Limited degree-of-freedom adaptive optics and image reconstruction," *Applied Optics*, vol. 30, pp. 4227-4233, 1991.

18. R. A. Wiggins, "Minimum entropy deconvolution," *Geoexploration*, vol. 16, pp. 21-35, 1978.

19. R. G. Lane and R. H. T. Bates, "Automatic multidimensional deconvolution," *J Opt Soc Am A*, vol. 4(1), pp. 180-188, Jan. 1987.

20. D. C. Ghiglia, L. A. Romero and G. A. Mastin, "Systematic approach to two-dimensional blind deconvolution by zero-sheet separation," *J Opt Soc Am A*, vol. 10(5), pp. 1024-1036, May 1993.

21. R. P. Millane, "Redundancy in multidimensional deconvolution and phase retrieval," *Digital Synthesis and Inverse Optics*, Arthur F. Gmitro, Paul Slidell, Ivan J. LaHaie, Eds., Proc. SPIE 1351, pp. 227-236, 1990.

22. B. Chalmond, "PSF estimation for image deblurring," *CVGIP: Graphical Models and Image Processing*, vol. 53(4), pp. 364-372, July 1991.

23. M. Cannon, "Blind deconvolution of spatially invariant image blurs with phase," *IEEE Trans Acoust, Speech, Signal Processing*, vol. 24(1), pp. 58-63, Feb. 1976.

24. M. M. Chang, A. M. Tekalp and A. T. Erdem, "Blur identification using the bispectrum," *IEEE Trans Signal Processing*, vol. 39(10), pp. 2323-2325, Oct. 1991.

25. B. Chalmond, "PSF estimation for image deblurring," *CVGIP: Graphical Models and Image Processing*, vol. 53(4), pp. 364-372, July 1991.

26. R. Fabian and D. Malah, "Robust identification of motion and out-of-focus blur parameters from blurred and noisy images," *CVGIP: Graphical Models and Image Processing*, vol. 53(5), pp. 403-412, Sept. 1991.

27. A. M. Tekalp, H. Kaufman and J. W. Woods, "Identification of Image and Blur Parameters for the Restoration of Noncausal Blurs," *IEEE Trans Acoust, Speech, Signal Processing*, vol. 34(4), pp. 963-972, August 1986.

28. R. L. Lagendijk, A. M. Tekalp and J. Biemond, "Maximum likelihood image and blur identification: a unifying approach," *Optical Engineering*, vol. 29(5), pp. 422-435, May 1990.

**Table 9: General Characteristics of Blind Deconvolution Methods for Images**

Class of Algorithms	Zero Sheet Separation	a priori Blur identification	ARMA Parameter Extraction	Nonparametric Deterministic Constraints Algorithms	HOS Methods
Assumptions about the true image	finite support	possibly contains edges or point sources	modeled by an AR process	deterministic constraints such as nonnegativity; support; blur invariant edges	accurately modelled by a non-Gaussian probability distribution
Assumptions about the blur	finite support	symmetric and non-minimum phase with a possibly known parametric form	symmetric and modeled by an MA process of a possibly known parametric form	IBD and SA: positive with known finite support; NAS-RIF: invertible	invertible
Complexity (order of the algorithm)	High	Very low (not iterative)	Moderate to high	Low to moderate; IBD: NAS-RIF:	Moderate
Convergence properties	sensitive to numerical inaccuracies; results in ill-convergence	not iterative	ill-convergence to local minima; sensitive to initial conditions	IBD: ill-convergence; sensitive to initial estimate; SA and NAS-RIF: converge to global minima	ill-convergence; sensitive to initial estimate
Sensitivity to additive noise	high	moderate to high	moderate	IBD: low; SA: moderate; NAS-RIF: moderate to high	low (Gaussian)
Most probable application areas	astronomy	astronomy; industrial x-ray imaging; photography	photography; texture image reconstruction	magnetic resonance imaging; positron emission tomography; x-ray imaging; astronomy	astronomy; seismic data analysis

29. R. L. Lagendijk, J. Biemond and D. E. Boekee, "Hierarchical blur Identification," *Proc IEEE Int Conf Acoustics, Speech, Signal Processing*, pp.1889-1892, 1990.
30. R. L. Lagendijk, J. Biemond and D. E. Boekee, "Identification and restoration of noisy blurred images using the expectation-maximization algorithm," *IEEE Trans Acoust, Speech, Signal Processing*, vol. 38(7), July 1990.
31. S. J. Reeves and R. M. Mersereau, "Blur identification by the method of generalized cross-validation," *IEEE Trans Image Processing*, vol. 1(3), pp. 301-311, July 1992.
32. C. M. Cho and H. S. Don, "Blur identification and image restoration using a multilayer neural network," *1991 IEEE Int Joint Conf on Neural Networks*, vol. 3, pp.2558-2563, 1991.
33. C. L. Nikias and A. P. Petropulu, *Higher-Order Spectral Analysis, A Nonlinear Processing Framework*, New Jersey: Prentice Hall, pp.282-295, 1991.
34. G. R. Ayers and J. C. Dainty, "Iterative blind deconvolution method and its applications," *Optics Letters*, vol. 13(7), pp. 547-549, July 1988.
35. B. L. K. Davey, R. G. Lane and R. H. T. Bates, "Blind deconvolution of a noisy complex-valued image," *Optics Communications*, vol. 69(5,6), pp.353-356, Jan. 1989.
36. N. Miura and N. Baba, "Extended-object reconstruction with sequential use of the iterative blind deconvolution method," *Optics Communications*, vol. 89, pp. 375-379, 1992.
37. N. Miura, N. Baba, S. Isobe, M. Noguchi and Y. Norimoto, "Binary star reconstruction with use of the blind deconvolution method," *Journal of Modern Optics*, vol. 39(5), pp.1137-1146, May 1992.

**Table 10: Table of Abbreviations**

Abbreviation	Name
AMD	absolute mean deviation
AR	autoregressive
ARMA	autoregressivemoving average
BIR	binary image of the words blind image restoration
CV	cross-validation
EM	expectation-maximization
FIR	finite impulse response
FFT	fast-Fourier transform
FT	Fourier transform
GCV	generalized cross-validation
HOS	high order statistics
HST	Hubble Space Telescope
IBD	iterative blind deconvolution (method)
LS	least-squares
MA	moving average
MED	minimum entropy deconvolution
ML	maximum-likelihood
MSE	mean square error
NAS-RIF	nonnegativity and support constraints recursive inverse filtering (method)
pdf	probability density function
PSF	point-spread function
SA	simulated annealing method)
SNR	signal-to-noise ratio
SNRI	signal-to-noise ratio improvement
toy	grey-scale image of a toy
UT	binary image of the letters UT
ZT	z-Transform

38. F. Tsumuraya, N. Miura and N. Baba, "Iterative blind deconvolution method using Lucy's algorithm," *Astron Astrophys.*, vol. 282(2), pp.699-708, Feb. 1994.
39. N. Miura, K. Ohsawa and N. Baba, "Single-frame blind deconvolution by means of frame segmentation," *Optics Letters*, vol. 19(10), pp.695-697, May 1994.
40. B. C. McCallum, "Blind deconvolution by simulated annealing," *Optics Communications*, vol. 75(2), pp.101-105, Feb. 1990.
41. S. Kirkpatrick, C. D. Gelatt Jr., and M. P. Vecchi, "Optimization by Simulated Annealing," *Science*, vol. 220, pp.671-680, 1983.
42. D. Kundur, "Blind deconvolution of still images using recursive inverse filtering," M.A.Sc. thesis, University of Toronto, Department of Electrical and Computer Engineering, 1995.
43. D. Kundur and D. Hatzinakos, "A novel recursive filtering method for blind image restoration," *IASTED Int Conf on Signal and Image Proc*, pp.428-431, Nov. 1995.
44. D. Kundur and D. Hatzinakos, "A Novel blind deconvolution scheme for image restoration using recursive filtering," submitted to *IEEE Trans on Signal Processing*, under review.

**Table 11: Table of Major Terms**

Term	Definition
Zero sheet separation	algorithms that perform blind deconvolution by factoring the two-dimensional ZT of the blurred image
<i>a priori</i> blur identification	algorithms that estimate the PSF priori to image restoration using known characteristics of the PSF and true image
ARMA parameter estimation	algorithms that model the blurred image using an ARMA model and perform deconvolution by estimating these parameters
Nonparametric deterministic constraints algorithms	algorithms that make deterministic assumptions about the image and PSF (examples: nonnegativity and finite support)
HOS methods	algorithms that make use of HOS information about the image for restoration

45. K. Nishi and S. Ando, "Blind superresolving image recovery from blur-invariant edges," *Proc IEEE Int Conf Acoustics, Speech, Signal Processing*, vol. 5, pp. 85-88, 1994.
46. R. G. Lane, "Blind deconvolution of speckle images," *J Opt Soc Am A*, vol. 9(9), pp. 1508-1514, Sept. 1992.
47. H. S. Wu, "Minimum entropy deconvolution for restoration of blurred two-tone images," *Electronics Letters*, vol. 26(15), pp. 1183-1184, July 1990.
48. G. Jacobitti and A. Neri, "A Bayesian approach to 2D non minimum phase AR identification," *Fifth ASSP Workshop on Spectrum Estimation and Modelling*, pp. 79-83, 1990.
49. A. H. Tewfik and H. Garnaoui, "Multigrid implementation of a hypothesis-testing approach to parametric blur identification and image restoration," *J Opt Soc Am A*, vol. 8(7), pp. 1026-1037, July 1991.
50. T. J. Holmes, "Blind deconvolution of quantum-limited incoherent imagery: maximum-likelihood approach," *J Opt Soc Am A*, vol. 9(7), July 1992.
51. J. Zhang, "The mean field theory in EM procedures for blind markov random field image restoration," *IEEE Trans Image Processing*, vol. 2(1), January 1993.
52. S. Haykin, ed., *Blind Deconvolution*, Prentice Hall, Englewood Cliffs, NJ, 1991.
53. J. L. Yen, "Image reconstruction in synthesis radiotelescope arrays," *Array Signal Processing*, S. Haykin, ed., Prentice Hall, Englewood Cliffs, NJ, pp. 293-350.
54. M. Z. Nashed, "Aspects of generalized inverses in analysis and regularization," *Generalized Inverses and Applications*, M. Z. Nashed, ed., Academic Press, New York: 1976.
55. N. B. Karayiannis and A. N. Venetsanopoulos, "Regularization theory in image restoration: the regularizing operator approach," *Optical Engineering*, vol. 28(7), pp. 761-780, July 1989.
56. P. D. Welch, "The use of the fast Fourier transform for the estimation of power spectra," *IEEE Trans Audio Electroacoust. (Special Issue on Fast Fourier Transform and its Application to Digital Filtering and Spectral Analysis)*, vol. 15, pp. 70-73, June 1967.
57. A. K. Jain, "Advances in mathematical models for image processing," *Proc IEEE*, vol. 69(5), pp. 502-528, May 1981.
58. G. H. Golub, M. Heath and G. Wahba, "Generalized cross-validation as a method for choosing a good ridge parameter," *Technometrics*, vol. 21, no. 2, pp. 215-223, May 1979.
59. V. A. Poliveira and J. M. Nightingale, "Maximum entropy image restoration in nuclear medicine," *Third International Conference on Image Processing and Its Applications*, pp. 669-673, July 1989.
60. R. M. Mersereau and R. W. Schafer, "Some techniques for digital deconvolution of positive constrained multi-dimensional sequences," *Proc 1978 European Conf Ciruit Theory and Design*, pp. 404-409, Sept. 1978.
61. R. M. Mersereau and R. W. Schafer, "Comparative study of iterative deconvolution algorithms," *Proc IEEE Int Conf Acoustics, Speech, Signal Processing*, pp. 192-195, Apr. 1978.
62. R. W. Schafer, R. M. Mersereau and M. A. Richards, "Constrained iterative signal restoration algorithms," *Proc IEEE*, vol. 69, pp. 432-450, Apr. 1981.
63. I. S. Stefanescu, "On the phase retrieval problem in two dimensions," *J Math Phys*, vol. 26, pp. 2141-2160, 1985.
64. W. H. Press, S. A. Toukolsky, W. T. Vetterling and B. P. Flannery, *Numerical Recipes in C, The Art of Scientific Computing*, 2nd ed., Cambridge University Press, New York: 1992.
65. A. K. Katsaggelos, M. G. Kang, and M. R. Banham, "Adaptive Regularized Restoration Algorithms Applied to HST Images," *Proc of 2nd Image Restoration Workshop*, pp. 3-13, Nov. 1993.